

## 1

## Measurement of Average Moisture Content and Drying Kinetics for Single Particles, Droplets and Dryers

*Mirko Peglow, Thomas Metzger, Geoffrey Lee, Heiko Schiffer, Robert Hampel, Stefan Heinrich, and Evangelos Tsotsas*

## 1.1

### Introduction and Overview

Knowledge of the amount of moisture contained in particles before, during and after drying is an elementary requirement in drying technology. This moisture amount, for example for quality control, can easily be determined on more or less large samples of particles by weighing.

However, other tasks, such as the design of industrial convective dryers impose much more serious challenges. To reliably design a convective industrial dryer, kinetic data referring to the specific product are necessary. Since information on drying kinetics is usually not available, it has to be gained experimentally. In this case, it is not sufficient to measure the mass of moisture contained in the product at a certain point of time, but the change of this mass with time has to be resolved as accurately as possible. Additionally, the change of mass with time must refer to the single particle. The reason for this second requirement is that gas conditions change in particle systems. This results – even if every particle has exactly the same properties and the particles are perfectly mixed – in more or less significant differences between the drying kinetics of the entire particle system and the drying kinetics of the single particle. Experimental techniques for the determination of single particle drying kinetics will be discussed in Section 1.2, with emphasis on the magnetic suspension balance.

On the other hand, it is evident that measurements on single particles will give only very low signals and, hence, be confronted with severe limitations of resolution and accuracy, even when using very sensitive instruments. This is especially true for small particles (powdery products). Therefore, we may be forced to investigate drying kinetics of an entire particle system such as a packed or fluidized bed. This is typically done by measuring gas humidity at the outlet of the dryer, instead of solids moisture content. It should be borne in mind that the results of such indirect measurements must be scaled down to the single particle by an appropriate model in order to obtain unbiased access to product-specific drying kinetics. Important instruments for

measuring gas humidity (infrared spectrometer, dew point mirror) will be presented in Section 1.3 along with some examples of scaling down.

Even if we are not interested in drying kinetics, but merely in quality control, measurement of the amount of moisture contained in a sample may not be sufficient. The reason is that the particles have a more or less broad residence time distribution in continuous dryers, which results in a moisture distribution in the outlet solids. This kind of distribution can only be resolved by measuring the moisture content of many individual particles. Methods for accomplishing this non-trivial task, namely coulometry and nuclear magnetic resonance, are the topic of Section 1.4. In the same section, an example of modeling the distribution of moisture in dried solids (in a population of particles) will be given.

Until Section 1.4 it is assumed that the product to be dried consists of solid particles containing moisture in their porous interior. While this is true for many drying processes, the feed of some others – namely spray drying – is a liquid. Determination of drying kinetics for the droplets cannot be conducted with the same methods as for solid particles, but requires the application of specific measuring techniques. This topic will be covered in Section 1.5 by detailed discussion of acoustic levitation.

Common to all the experimental techniques of the present chapter is that they do not provide immediate access to the moisture profiles developing in the interior of particles, droplets or other bodies during drying. Direct measurement of such profiles requires other experimental approaches, which will be presented in Chapters 2–4.

## 1.2

### Magnetic Suspension Balance

#### 1.2.1

##### Determination of Single Particle Drying Kinetics – General Remarks

Before presenting the magnetic suspension balance as a modern instrument for measuring single particle drying kinetics a short review of other methods, which can be used for the same purpose, will be given. These involve the use of

- a conventional microbalance
- a balance in combination with a drying tunnel
- an acoustic levitator.

A straightforward method to measure a drying curve is to put one wet particle on a conventional microbalance and record its change in weight (Hirschmann and Tsotsas, 1998). To avoid heat transfer from the plate of the balance, a miniature wooden stand can be used. The particle is fixed in the crossbeam of this stand between the sharp tips of very thin wood bars. In this way, it is surrounded by air, providing uniform heat and mass transfer from all sides. However, such measurements are limited to ambient conditions and difficult to reproduce exactly.

When hanging the specimen in a drying tunnel, connection to the balance must be provided by means of a cord or thin wire. Since forces and force fluctuations are transferred in this way from the specimen to the balance, a certain noise in the data is unavoidable, so that it does not make sense to use the most accurate microbalance. Therefore, a common balance with a sensitivity of merely 0.1 mg was used by Groenewold *et al.* (2000). The specimen consisted of 50 particles glued at sufficient distance from each other on a net of watertight material, as proposed by Blumberg (1995). Due to the distance between the individual particles, the measurement can be assumed to closely approximate single particle kinetics.

Experiences with the mentioned gravimetric methods are summarized in Tab. 1.1. As this table shows, both methods are limited with respect to operating conditions such as gas temperature and gas velocity. Measurement up to the relatively high gas velocity of  $2 \text{ m s}^{-1}$  indicated in Tab. 1.1 for the drying tunnel is possible only by post treatment of the primary experimental results. This smoothing has been performed by averaging and a cubic spline, as proposed by Kemp *et al.* (2001). A serious further limitation concerns the minimum size of particles that can be investigated – due to both balance accuracy and difficulties in handling and fixing objects smaller than about 1 mm. Co-axial flow with respect to the hanging sample (DaSilva and Rodrigues, 1997; Looi *et al.*, 2002) may have some advantages in comparison to cross-flow against the specimen in the drying tunnel, but it is not fundamentally different.

The difficulty common to all gravimetric methods arises from the requirement of suspending the particle in gas while simultaneously measuring its weight by connection to a balance. One solution is to refrain from gravimetric measurement and concentrate all efforts in reasonably suspending the particle in a flow field. This leads to acoustic levitation. The principles of acoustic levitation and its application to droplets will be discussed in detail in Section 1.5. Here, it should just be mentioned that the method has also been applied for particles by Groenewold *et al.* (2002) using a closed 45 kHz instrument. For better stability, a liquid droplet was suspended first and the wet particle was then placed in this droplet. To determine the evaporation rate a small air purge was applied, and the change of outlet air humidity was measured by means of a high accuracy dew point mirror. This is very similar to the procedures that will be discussed in Section 1.3. Experiences from these measurements are also summarized in Tab. 1.1. They reflect problems of stability of suspension at high

**Tab. 1.1** Applicability of different methods for the determination of single particle drying kinetics according to Kwapinski and Tsotsas (2006).

Method	$d_p$ , mm	$T$ , °C	Flow velocity, $\text{m s}^{-1}$
Microbalance	min. 1	20–30	~0
Drying tunnel	min. 1	30–60	max. 2
Levigator	1–2	max. 30	0.02–0.065
Magnetic suspension balance	min. 1	max. 350	max. 1

temperatures and strong purges, which would evidently destroy the oscillating pressure field and, thus, also the suspension force acting on the particle.

An alternative strategy is to still use a balance, but refrain from any material connection between specimen and weight measuring cell. The realization of this idea in a magnetic suspension balance will be discussed in the following.

### 1.2.2

#### Configuration and Periphery of Magnetic Suspension Balance

A schematic representation of the principle of a magnetic suspension balance (MSB) is shown in Fig. 1.1. As already mentioned, the force to be measured is transmitted in a contactless way from the specimen to the microbalance. This is achieved by means of a magnetic force coupling, consisting of an electromagnet and a permanent magnet. The fact that the measuring device is disconnected from the sample chamber enables the microbalance to be kept always under ambient conditions, while high temperatures (up to 350 °C) and high pressures (up to 500 kPa) may be realized in the sample chamber.

The MSB used by the authors was produced by Rubotherm (Bochum, Germany). It is equipped with a feature called measuring load decoupling, which is conducted by first lowering the suspension magnet in a controlled way to a second stationary position a few millimeters below the measuring position. Then, a small carrier to which the sample is connected is set down on a support. Now the sample is decoupled from the balance. The suspension magnet is in a freely suspended state, and only its own weight is transmitted to the balance. This so-called zero point position, which corresponds to an empty balance pan in a normal weighing procedure, allows for taring and calibration of the balance at all times, even when recording measurements

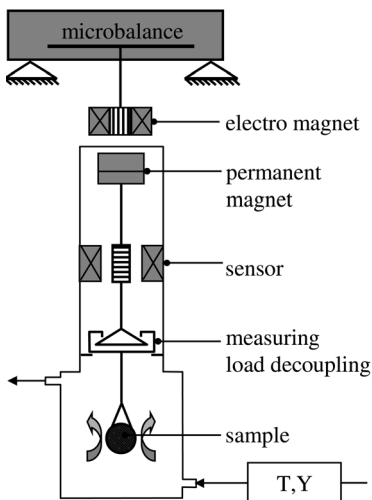


Fig. 1.1 Schematic representation of the MSB.

under process conditions in the measuring cell. The resulting correction of zero point and sensitivity drifts increases the measuring accuracy significantly, especially in the case of long term measurements (Rubotherm, 2004). Apart from drying kinetics, chemical reactions (polymerization, decomposition, combustion, corrosion), formulation processes (e.g. coating), phase equilibrium (e.g. sorption) and material properties (surface tension, density) can also be investigated in the MSB.

The configuration installed in the laboratory of the authors (Fig. 1.2) is used mainly for determination of drying kinetics or sorption equilibrium. Therefore, it includes a periphery capable of establishing different atmospheres of conditioned air. The design of this humidifier is identical to the set-up for calibration of IR spectrometers that will be described in Section 1.3.4. Additionally to the measurement of weight, gas humidity can be measured at the inlet of the MSB (after the air conditioner) and at the outlet of the MSB by means of a dew point hygrometer and an IR spectrometer, respectively. The gas feed can be pressurized air with a moisture content of  $0.5 \text{ g kg}^{-1}$  or completely dry flask gas. Mass flow rates are adjusted by a mass flow controller, calibrated by means of a film flow meter.

A correction for buoyancy should be applied to MSB data according to the relationship (Rubotherm, 2004):

$$M_L = M_{BL} + V_L \cdot \rho_g \quad (1.1)$$

Here,  $M_L$  and  $V_L$  are the mass and volume of the load (including load cage and basket), respectively;  $M_{BL}$  is the value of the balance display and  $\rho_g$  is the gas density.

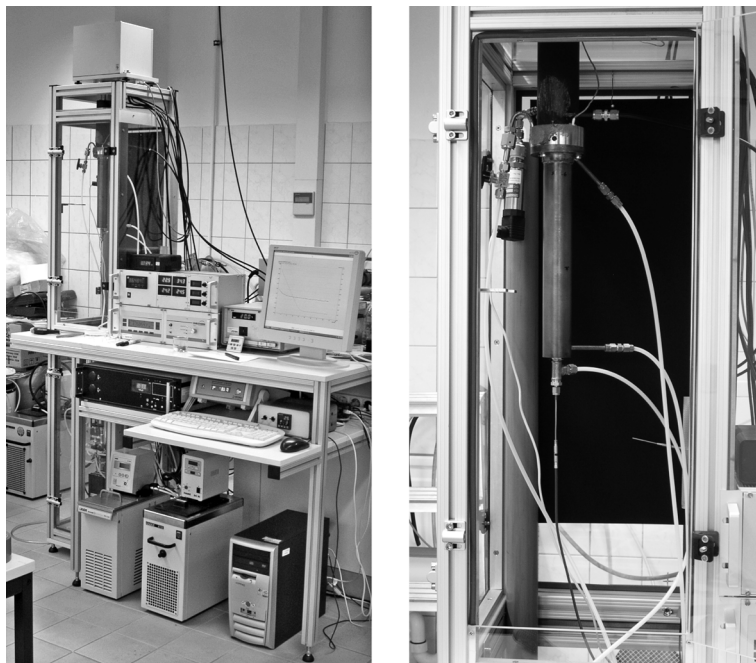


Fig. 1.2 Experimental set-up of magnetic suspension balance (MSB).

Furthermore, for drying samples in the range of milligrams the buoyancy of the sample should be taken into account. Thus, the expression

$$M_S = M_{BLS}(P, T, \varphi) - M_{BL}(P, T, \varphi) + V_S \cdot \rho_g(P, T, \varphi) \quad (1.2)$$

can be used to calculate the mass of the sample,  $M_S$ . Here,  $M_{BLS}$  is the value that the balance displays with sample,  $M_{BL}$  is the value that the balance displays without sample and  $V_S$  is the volume of the dry sample. The influence of changing state variables in the sample chamber (pressure  $P$ , temperature  $T$ , relative humidity  $\varphi$ ) is considered in Eq. 1.2. However, the buoyancy effect contributed by water (moisture), which is usually less than  $1 \mu\text{g}$ , is neglected.

### 1.2.3

#### Discussion of Selected Experimental Results

In the following, applications of the magnetic suspension balance are illustrated on the basis of results by Kwapinski (Kwapinski and Tsotsas, 2004a, b, 2006). The materials used in these experiments (molecular sieve 4A,  $\gamma\text{-Al}_2\text{O}_3$  and SiC) have very different pore diameters, see Tab. 1.2. Zeolite and alumina oxide are highly hygroscopic, while silicium carbide has very low hygroscopicity.

Figure 1.3, as an example, shows results on the kinetics of desorption of water from one single particle of zeolite 4A. This particle with a diameter of 2 mm was fixed with glue onto the tip of a thin needle suspended in the sample chamber of the MSB. First, water was adsorbed on the particle by exposing it to air with a relative humidity of  $\varphi_0 = 0.60$ . Then, the experiment was started by suddenly reducing the relative humidity of the air from this initial value to a value of  $\varphi_{in} = 0.05$  at the inlet of the sample chamber. The progress of particle moisture content until reaching the new, lower equilibrium value is plotted in Fig. 1.3 for different gas velocities. To obtain results representing the kinetics of mass transfer in the interior of the particle, it is desirable to reduce the relatively small influence of gas-side mass transfer as far as possible by measuring at high gas velocities. This, however, has an adverse effect on the accuracy of weighing, so that a compromise must be found. In this context, it should be mentioned that the flow of conditioned air during the presented experiments was from the bottom to the top of the sample chamber. This creates a flow force on the particle – similar to the buoyancy force. Consequently, smaller indications of mass are obtained by the balance with increasing flow velocity. The resulting minor error can be corrected by calibration, so that weighing results independent of flow

Tab. 1.2 Selected properties of experimental materials.

	zeolite 4A	$\gamma\text{-Al}_2\text{O}_3$	SiC
$d_p$ , mm	2.0 and 5.0	1.4	1.0–1.8
$d_{\text{pore}}$ , $\mu\text{m}$	0.0004	0.01	0.12–5.1
$\rho_p$ , $\text{kg m}^{-3}$	720	1040	1610–2330
$e_p$ , %	33.5	70–75	25–49

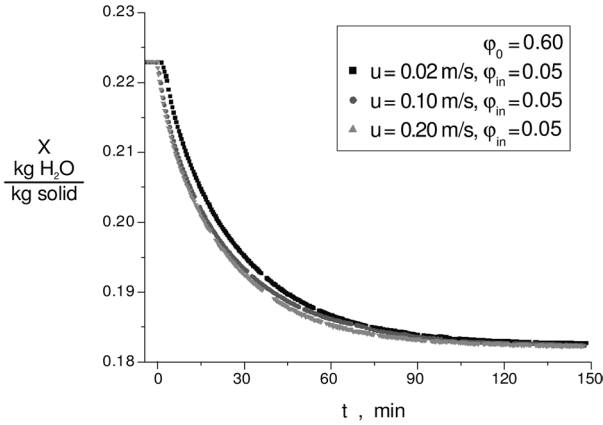


**Fig. 1.3** Experimental desorption curves of water from 4 A zeolite at 25 °C; Comparison of process kinetics for different velocities of the air.

velocity are obtained. Even without correction, the results are sufficient for many practical applications.

The results of similar experiments with a single particle of  $\gamma\text{-Al}_2\text{O}_3$  are depicted in Figs. 1.4 and 1.5. Here, the ordinate shows directly the mass, which decreases during desorption of water. The relative random error of measurement by the MSB is indicated. This error increases with increasing gas flow velocity, but is still reasonably small at  $u = 0.2 \text{ m s}^{-1}$ . On the other hand, such a velocity is sufficient for the process to take place in the particle-side controlled regime. Experiments with bigger particles

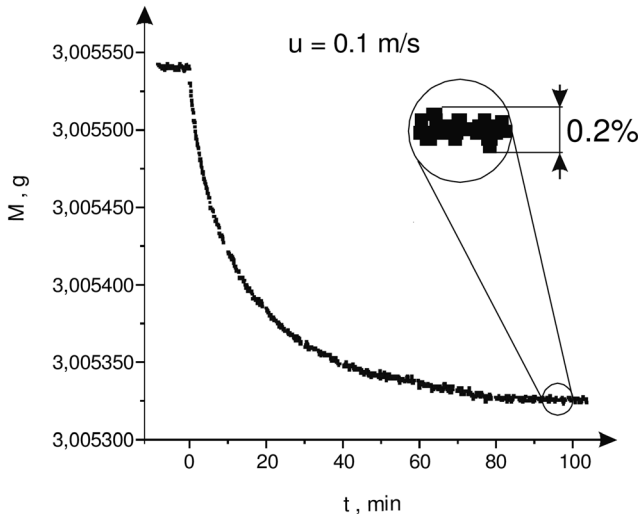


**Fig. 1.4** Desorption of water from  $\gamma\text{-Al}_2\text{O}_3$  in the MSB at  $u = 0.1 \text{ m s}^{-1}$ ; ( $T = 25 \text{ }^\circ\text{C}$ ,  $\varphi_0 = 20\%$ ,  $\varphi_{in} = 5\%$ ).

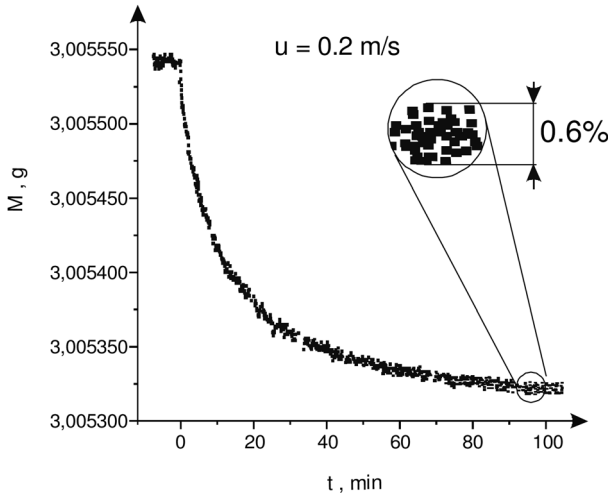


**Fig. 1.5** Desorption of water from  $\gamma\text{-Al}_2\text{O}_3$  in the MSB at  $u = 0.2 \text{ m s}^{-1}$ ; ( $T = 25 \text{ }^\circ\text{C}$ ,  $\varphi_0 = 20\%$ ,  $\varphi_{in} = 5\%$ ).

revealed that the relative error increases with particle size for the same gas velocity. The reason is the larger vibrations of large particles. Though still occurring, such vibrations are better damped in the MSB than in other gravimetric devices, due to the indirect contact by the suspension magnet.

The mentioned relative error also depends on the moisture load, which is changing during the desorption process, and differs for different particle sizes and materials. Figure 1.6 presents results for the materials of Tab. 1.2 under otherwise the same conditions. All materials were conditioned at  $T = 25 \text{ }^\circ\text{C}$  and  $\varphi_0 = 0.30$ . At  $t = 0$  there was a sudden change of relative humidity of the flowing air to  $\varphi_{in} = 0.05$ . The amount of water that can evaporate from zeolite is defined as unity in Fig. 1.6 and is larger than for the two other materials. The relative error for SiC, with a total water loss of

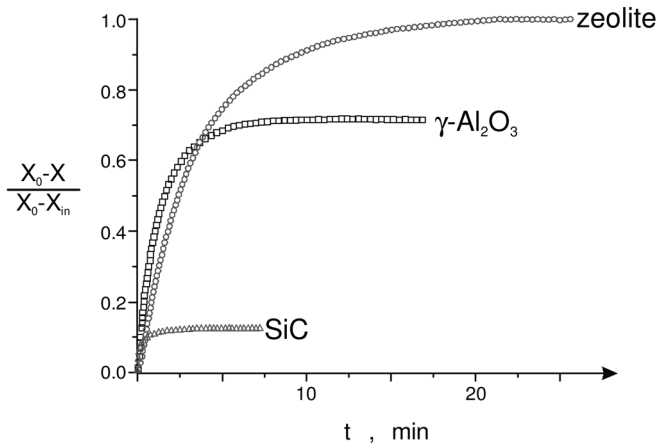


**Fig. 1.6** Desorption data for zeolite 4A,  $\gamma\text{-Al}_2\text{O}_3$  and SiC.

about 10 times less than zeolite, will be proportionally larger. This ratio is not constant, but depends on the operating conditions. It should, however, be pointed out that SiC is usually considered to be completely non-hygroscopic. In fact, the weak hygroscopicity indicated by Fig. 1.6 could not be detected by conventional gravimetric methods, but can be detected in the MSB.

Using the MSB it is also possible to gain equilibrium data. Examples of isotherms for the adsorption of water on molecular sieves are shown in Fig. 1.7. In such experiments, more than one particle may be placed into a basket, suspended from the balance. Even with many particles in the basket, the time to reach a constant mass is much shorter than required by conventional methods, due to the favorable flow of conditioned air. The temperature range of Fig. 1.7 can be widened to 350 °C. Such high temperatures and vacuum may be necessary to determine the mass of “dry” particles, that is, the reference in the definition of solids moisture content. To find this mass, experiments as depicted in Fig. 1.8 were made. Initially, the temperature should be raised slowly to 100 °C in an environment of N<sub>2</sub>. After 100 °C the temperature can be increased more quickly. In the presented experiment this was done stepwise. The temperature trajectory should, ideally, be piecewise linear, but, in reality, some inertial effects and overshooting are present. The final measurement was taken at 350 °C and in vacuum, after the mass had reached a constant value. The change of condition at the end of the experiment from dry gas at ambient pressure and small flow to vacuum is the reason for the small jump in the mass indication. This is due to the removal of the flow and represents the small inaccuracy that has been previously discussed and can be corrected by calibration.

Recent work (Suherman, 2007; Suherman *et al.*, 2008) shows that the drying kinetics of single polymer granules with diameters from 2.5 to 2.9 mm can be measured with good reproducibility by using the MSB. The accuracy of the instrument under specific operating conditions can be evaluated by time series analysis and other statistical methods. Furthermore, it is shown in this work how the time series analysis can contribute to a reliable identification of the end of the drying process.

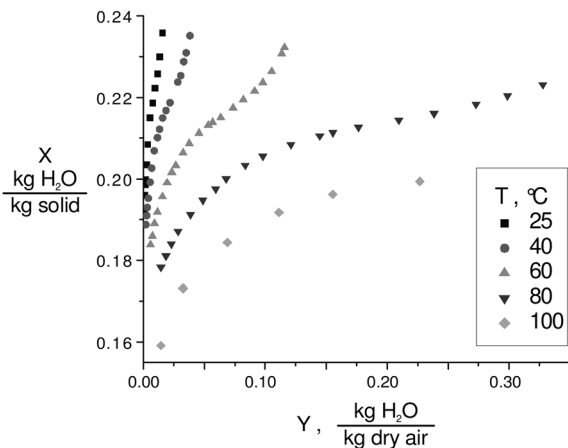


Fig. 1.7 Isotherms for adsorption of water on zeolite 4 A.

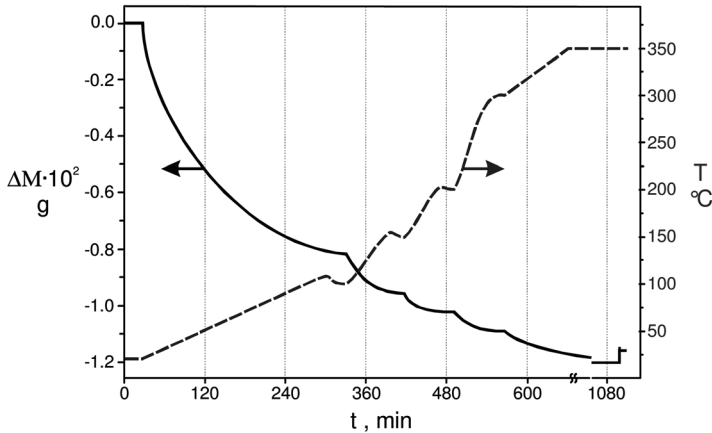


Fig. 1.8 Measurement for the determination of the mass of dry zeolite by use of the MSB.

This helps to accurately determine dry mass. Statistical methods can also support data smoothing. Instead of the previously mentioned cubic splines, Suherman (2007) used the moving average technique to this purpose. By smoothing the primary data the significance of measurements can be extended towards smaller moisture contents at the end of the drying process.

A coarse estimation of the applicability range of the MSB is given in Tab. 1.1. Concerning this table, it should be noticed that the maximum operating velocity of  $u = 2 \text{ m s}^{-1}$  assigned to the drying tunnel could be attained only in combination with numerical smoothing of the primary data. In contrast, gas velocities of up to  $u = 1 \text{ m s}^{-1}$  can be realized in the MSB without smoothing. Without smoothing, the MSB has an advantage with regard to the maximum possible gas velocity.

Nevertheless, such information is only indicative, because the applicability range shrinks unavoidably with decreasing particle diameter, due to the decrease in weight. Additionally, it becomes more and more difficult to fix one particle without significant contact with some solid support. Consequently, the applicability of all gravimetric methods – including the MSB – ends at a particle diameter of about 1 mm. For powdery materials with much smaller particle size alternative methods are needed. Such alternatives will be discussed in the following section.

### 1.3

#### Infrared Spectroscopy and Dew Point Measurement

##### 1.3.1

##### Measurement for Particle Systems – General Remarks

As discussed in the previous section, the determination of the drying kinetics of materials with a particle size below 1 mm can hardly be conducted by single particle experiments; the accuracy and resolution of the methods available for this purpose

are not high enough. Consequently, it is necessary to measure the temporal change in moisture content of an entire particle system and then extract from this information single particle drying kinetics. The particle systems considered are packed beds and fluidized beds.

The use of a packed bed corresponds to the well known thin layer method (TLM, see, e.g. Hirschmann *et al.*, 1998). In TLM a shallow packed bed is placed on a sieve with air flow in the direction of gravity. The moisture content of the packed bed is measured by interrupting the experiment and weighing. Alternatively, outlet gas humidity can be measured and used to calculate the corresponding change in the moisture content of the solids. Even for very thin layers the results of this method cannot be set equal to single particle drying kinetics, but have to be scaled-down to the single particle by an appropriate model. Such modeling is not trivial, due to axial dispersion in the gas flowing through the packed bed. Additionally, it is difficult to prepare a particle layer of small but uniform thickness. Differences in thickness lead, however, to flow maldistribution, because the gas prefers pathways of minimal bed thickness and, thus, minimal flow resistance. Such flow bypasses can hardly be modeled. Moreover, they depend on the skills of the person who has prepared and conducted the experiment.

Gas bypass is also present in a fluidized bed, due to bubbling. However, this bypass is a property of the particle system – rather independent from the operator. Furthermore, reliable models are available for scaling fluidized bed drying results to the single particle. Because of these advantages, the route from fluidized bed measurements to single particle drying kinetics will be discussed in detail in this section.

The first step is the determination of the change in solids moisture content in the fluidized bed with time. Conventionally, one takes samples out of the bed during the drying process and measures the moisture content by weighing. This is intermittent, changes the hold-up and provides just a few points along the drying curve of the fluidized bed. Therefore, it is better to determine the decrease in solids moisture content in the fluidized bed dryer indirectly, by measuring the gas moisture content at the outlet. For the simple case of a batch dryer one needs to quantify the moisture content of the gas at the inlet and at the outlet of the dryer and the mass flow rate of the dry fluidization gas. The evaporation flow rate is then given by

$$\dot{M}_v = \dot{M}_g(Y_{\text{out}} - Y_{\text{in}}) \quad (1.3)$$

Taking into account the initial moisture content of the solids  $X_0$ , the temporal change of moisture can be determined from

$$X(t) = X_0 - \frac{1}{M_{\text{dry}}} \int \dot{M}_g(Y_{\text{out}} - Y_{\text{in}}) dt \quad (1.4)$$

Obviously, the measurement of the gas moisture contents  $Y_{\text{out}}$  and  $Y_{\text{in}}$  determines the quality of the method. Before discussing this measurement, by infrared spectroscopy and dew point determination, a short outline of the experimental set-up will be given.

## 1.3.2

**Experimental Set-Up**

A schematic diagram of the laboratory scale fluidized bed dryer used in our work is presented in Fig. 1.9. The cylindrical fluidization chamber has an inner diameter of 152 mm. A sintered metal plate with a pore size of 100  $\mu\text{m}$  serves as the air distributor in order to ensure a uniform flow of fluidization gas. To control the gas inlet temperature the apparatus is equipped with an electrical heater. For granulation or agglomeration processes a two-component nozzle with an adjustable gas flap (Type 970/0 S4, Schlick Co.) is installed. The liquid is delivered to the nozzle by a piston pump (Sewald Co.). Pressurized air is used as the fluidization gas in order to attain as constant as possible flow rates. In this way, the variation of mass flow rate could be kept below  $\pm 0.1 \text{ kg h}^{-1}$ . Using a blower would lead to significantly higher fluctuations. The gas flow rate is measured by means of a mass flow meter (ELFLOW, Bronkhorst Mättig Co.). Additionally, several probes are installed to record temperatures at the gas inlet and outlet, and pressure drops of the distributor plate and the hold-up.

As mentioned above, the accuracy of the described approach depends directly on the precision of the measurement of gas moisture content. This requires

- high accuracy
- short measurement period.

Both requirements can be fulfilled by employing infrared (IR) spectroscopy. In our case, two IR spectrometers of type NGA 2000 MLT (EMERSON Process Management Co.) were installed at the inlet and at the outlet of the fluidization chamber.

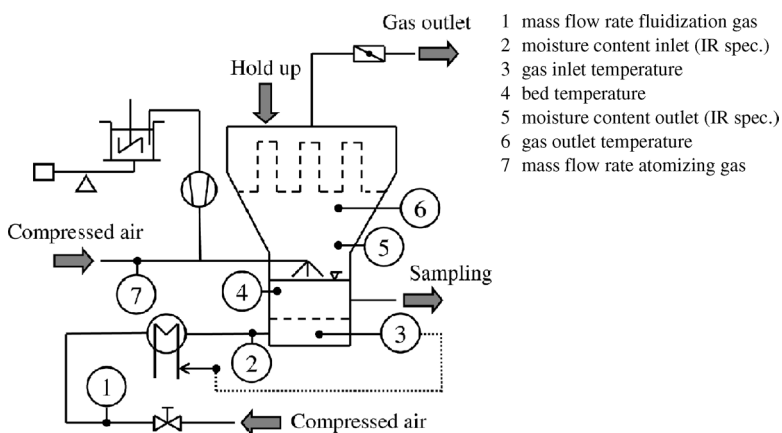


**Fig. 1.9** Scheme of fluidized bed dryer.

## 1.3.3

**Principle of Measurement with the Infrared Spectrometer**

The basis of IR spectroscopy is absorption of infrared radiation caused by the gas being measured. While the wavelengths of the absorption bands are specific to the type of gas, the strength of absorption is a measure of concentration. By means of a rotating chopper wheel, the radiation intensities coming from the measuring and the reference sides of the cell of the instrument produce periodically changing signals within a detector. The detector signal amplitude thus alternates between concentration dependent and concentration independent values. The difference between the two is a reliable measure of the concentration of the absorbing gas component.

Figure 1.10 depicts a scheme of the IR spectrometer. A heating coil in the light source (1) generates the necessary infrared radiation. This radiation passes through the light chopper wheel (2) and a filter cell (4) that screens interfering wavelengths out of the radiation spectrum. Due to the shape of the chopper wheel, irradiation of equal intensity alternates between the measuring side (6) and the reference side (7) of the analysis cell (5). Only the measuring side is swept by the gas to be analyzed. Subsequently, the radiation passes individual optical filters around a second filter cell (8) and reaches the pyro-electrical detector (10). This detector compares the measuring side radiation, which is reduced because of absorption by the gas, and the

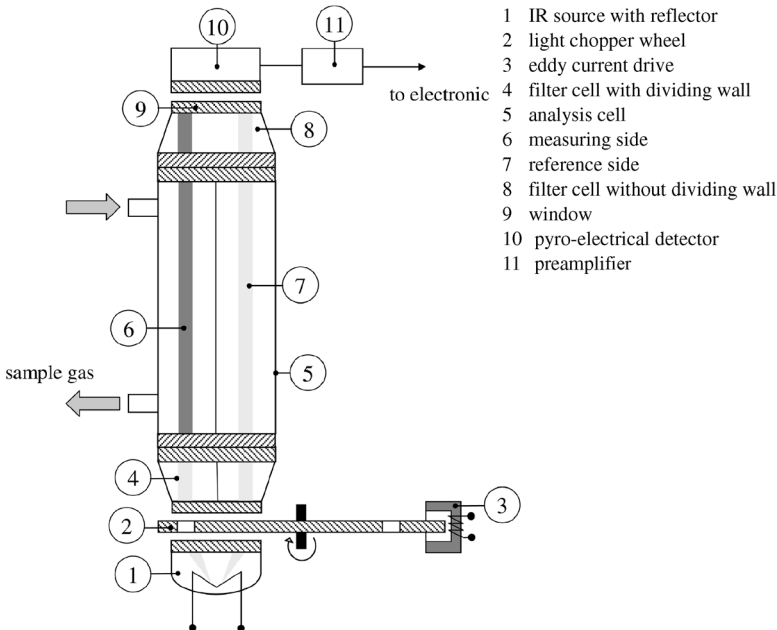


Fig. 1.10 Scheme of IR spectrometer.

reference side radiation. Cooling and heating of the pyro-electrical material of the sensor lead to an alternating voltage signal. The final measuring signal of the IR spectrometer is equivalent to the volume concentration of the absorbing gas component. In our case, this component is water vapor. Volume concentration is equal to molar fraction  $\tilde{y}$ , which can be converted into the mass moisture content by the relationship

$$Y = \frac{\tilde{M}_w \tilde{y}}{\tilde{M}_g (1 - \tilde{y})} \quad (1.5)$$

### 1.3.4

#### Dew Point Mirror for Calibration of IR Spectrometer

To achieve the highest precision for the determination of the moisture content in the gas phase the IR spectrometers need to be calibrated frequently since the pressure in the measuring chamber and, therefore, also the measured volume concentration of water, depend on the ambient pressure. For the calibration, a gas flow with defined moisture content must be supplied to the IR spectrometers. The accuracy of calibration of the spectrometers will depend directly on the accuracy of the measurement of moisture of the provided calibration gas. Dew point mirrors are amongst the most established and recognized devices for the precise determination of moisture content in gases, because of their simplicity and the fundamental principle employed. From the measured dew point temperature  $T_{dp}$ , the saturation pressure  $p^*$  of the water and hence the moisture content can be acquired:

$$Y = \frac{\tilde{M}_w p^*(T_{dp})}{\tilde{M}_g P - p^*(T_{dp})} \quad (1.6)$$

In a dew point instrument a gas sample is conducted into the sensor cell that contains a miniature temperature-controlled polished metal mirror (Fig. 1.11). This

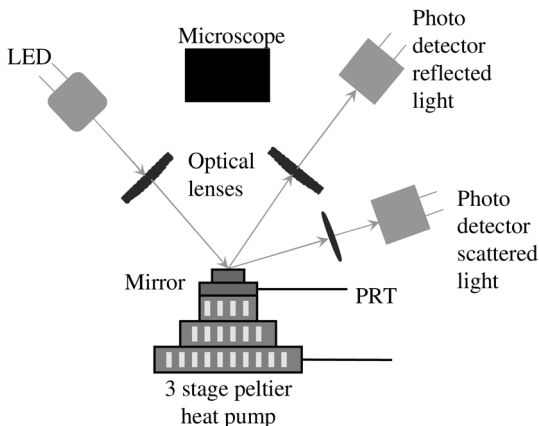


Fig. 1.11 Operating principle of a dew point mirror.

mirror is made of a highly conductive material, typically copper, and plated with an inert material such as gold. It sits on a solid-state thermoelectric heat pump cooling by means of the Peltier effect.

As the temperature of the mirror drops and reaches the dew (or frost) point temperature, water is pulled out of the vapor phase of the sample gas and water droplets (or ice crystals) nucleate on the mirror's surface to form eventually a uniform condensation layer. The exact temperature, measured by a platinum resistance thermometer (PRT) directly embedded underneath the mirror's surface, depends only upon the moisture content of the gas and the operating pressure.

An optical system, consisting of a visible light emitting diode (LED) and photodetectors, is used to detect the point at which this occurs. The LED provides a light beam of a constant intensity, which is focused by a collimated lens to become the incident beam on the mirror surface, flooding it with a pool of light. Some instruments only detect the reflected light using a single photodiode; more sophisticated instrumentation uses a second detector to monitor the scattered light.

As dew droplets form on the mirror, the reflected light decreases whilst the amount of scattered light increases. The output from each photodiode is digitized with an analog to digital converter to derive numerical representations of the photodetectors. The resulting signals are, in turn, tied into an electronic loop that controls the current applied to the heat pump device. This, in essence, modulates the cooling power to maintain the mirror temperature at the dew (or frost) point of the gas sample.

At an equilibrium point, where evaporation rate and condensation rate at the surface of the mirror are equal, the mirror temperature, read by the PRT embedded in the mirror, represents the saturation point for the water vapor in the sample gas, in other words the dew (or frost) point.

Whilst the combined condensation of water-soluble gas constituents may be acceptable in small amounts, accumulation of such contaminants over an extended period of time can affect the accuracy of the measurement. Cooled mirror hygrometers usually have the facility to execute a contamination compensation routine to prevent this effect. When the system initiates the dynamic contamination control (DCC) routine, the heat command signal drives the thermoelectric heat pump in reverse, which in turn heats the mirror to a temperature above the dew point to drive off the excess condensate. When the mirror is free from condensation, the optical control loop is typically zeroed to eliminate the effect of contaminants, which may have built up on the mirror surface. Following this re-zeroing of the optical control loop, normal operation of the device is resumed.

For mirror temperatures above 0 °C, water vapor condenses on the mirror as liquid water (dew point). When measuring temperatures are below the freezing point of water, the condensate can either exist as ice (frost point) or as super-cooled liquid (dew). Whether the condensate is ice or water depends on several factors, such as the purity of the water, the surface morphology of the mirror and the period of time over which the measurement has been made. Alternatively, because of delayed nucleation the condensate may initially appear as a liquid (water) but change into a solid (ice) after a certain period of time.

For water to freeze, the molecules must become properly aligned to each other, so that it is more difficult to liberate a molecule from ice than from super-cooled liquid water. Therefore, different saturation temperatures are measured for super-cooled water and ice, the former being lower than the latter. This phenomenon affects all cooled mirror instruments and may result in inaccurate interpretation. If the condensate present over a mirror is ice, the mirror temperature at equilibrium will be higher than if the condensate were super-cooled liquid. The errors involved are typically about 10% of water vapor pressure. In order to distinguish between water and ice, some hygrometers are equipped with a microscope which allows the user to visually inspect the surface of the mirror during measurement and look for frost or dew formation. However, the addition of a microscope is usually an expensive option, and it can be difficult to discern water from ice formation, particularly at low dew point temperatures.

In the present work an Optidew Vision (Michell Instruments Co.) dew point mirror was used. The measuring range of this dew point hygrometer is from  $-30$  to  $50$  °C with an accuracy of 0.2 K. It is integrated in a device for calibration of IR spectrometers, as depicted in Fig. 1.12. The NGA 2000 IR spectrometer can be calibrated with a simple two-point calibration, since the signal from the pyro-electric sensor is assumed to be linear within the measuring range. Synthetic air from the flask with a dew point of  $-30$  °C was used as the so-called zero-gas. The second calibration point was obtained by moistening the synthetic air in a fritted wash bottle to adjust to a dew point of approximately  $21$  °C. The measuring conditions in the analysis cell of the IR spectrometer were controlled in such a way that a gauge pressure of 5 mbar and a flow rate of the sample gas of  $400$  ml  $\text{min}^{-1}$  were attained. The flow rate was determined by means of a film flow meter (Type SF-2CE, Horiba Stec Co.). The actual values of gas moisture were quantified by means of the dew point mirror for both calibration points.

According to the manufacturer, the accuracy of the IR spectrometer is 1% of the final value of the upper limit of the measuring range. By default, the measuring range is set from 0 to 10% volume concentration of water vapor. To increase the accuracy, the upper limit of the measuring range was reduced to 2.8%, which corresponds to a moisture content of  $17.92$  g  $\text{kg}^{-1}$ . Consequently, the accuracy of measurement of volume concentration is increased to  $\pm 0.028\%$  so that the moisture content can be

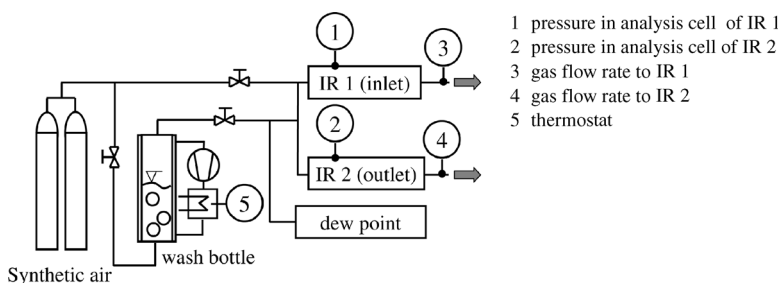


**Fig. 1.12** Scheme of the calibration device.

Tab. 1.3 Measured moisture contents for justification of the linearization.

Dew point [°C]	Y (dew point) [g kg <sup>-1</sup> ]	Y (IR) [g kg <sup>-1</sup> ]
15.85	11.25	11.26
11.35	8.35	8.39
6.65	6.06	6.16

determined with an accuracy of approximately  $\pm 0.18 \text{ g kg}^{-1}$ . To prove the linearization of the IR spectrometer three additional dew points were adjusted directly after the calibration. The results, summarized in Tab. 1.3 and depicted in Fig. 1.13, demonstrate that the linear calibration is very satisfactory for the measurement of moisture content. The deviation of the values obtained from the IR spectrometer and the dew point mirror is less than the accuracy of  $\pm 0.18 \text{ g kg}^{-1}$ .

### 1.3.5

#### Testing the Calibration

As mentioned above, the closure of water balance is essential for the determination of solids moisture content. The closure does not only depend on the measurement of gas humidity but also on the precise determination of gas flow rate and liquid flow rate, whereby the latter is important only in the case of agglomeration and granulation processes. In principle, there are two simple methods to assess the overall accuracy of the instrumentation. The first method is a differential approach, where a certain liquid flow rate is injected onto the particles and the instantaneous evaporation rate is quantified. Under steady state conditions the evaporation rate must be equal to the spraying rate

$$\dot{M}_l = \dot{M}_v = \dot{M}_g(Y_{\text{out}} - Y_{\text{in}}) \quad (1.7)$$

For the tests the mass flow rate of the fluidization gas and atomizing air of the nozzle was adjusted to  $50.61$  and  $0.89 \text{ kg h}^{-1}$ , respectively. To minimize the transition time to steady state, non-hygroscopic  $\alpha\text{-Al}_2\text{O}_3$  with a Sauter mean diameter  $d_{32} = 0.31 \text{ mm}$  was used as the bed material. Fig. 1.14a shows the temporal change of gas moisture

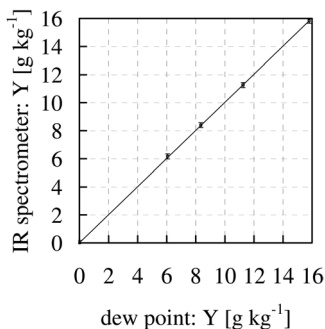
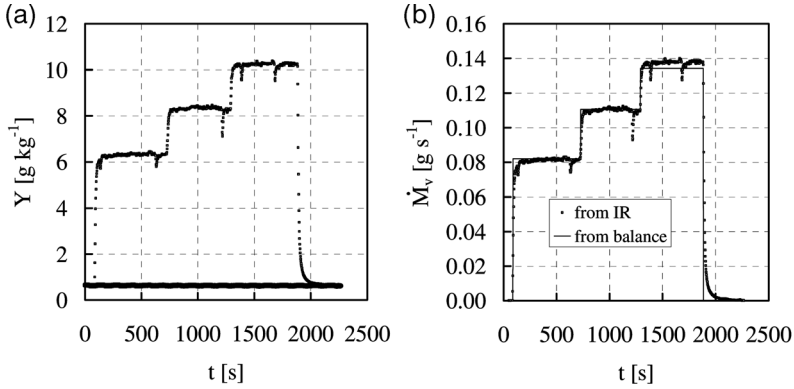


Fig. 1.13 Results for testing the linearization of the IR spectrometer.



**Fig. 1.14** Experimental results for testing the differential water balance at spraying rates of 0.082, 0.110 and 0.134 g s<sup>-1</sup>; (a) temporal change of gas moisture content; (b) comparison of evaporation rate from the IR spectrometer with gravimetrically determined spraying rate.

obtained for the three different spraying rates which are summarized in Tab. 1.4. The occasional sharp decrease in outlet moisture content is caused by the switching of the pistons of the pump that feeds water to the nozzle. When this happens, the liquid flow is interrupted for 1 to 2 s, which is readily detected by the spectrometer. Figure 1.14b presents the comparison of the actual spraying rate with the evaporation rate determined by applying Eq. 1.7. As one can see, the deviation is very low. Only for the highest spraying rate was a slight systematic difference observed.

To quantify the error of the differential balance, the deviation of spraying rate from evaporation rate

$$\Delta \dot{M}_v = \dot{M}_l - \dot{M}_g(Y_{out} - Y_{in}) \quad (1.8)$$

is presented in Fig. 1.15 for undisturbed steady state conditions. As one can see, the error of the differential balance is approximately  $\pm 2 \text{ mg s}^{-1}$  for the first two spraying rates, but increases slightly and becomes systematic for the highest spraying rate. The resulting deviations are summarized in Tab. 1.4. In total, it can be concluded that the differential balance is successfully closed, so that the instantaneous evaporation rate can be determined with an accuracy of approximately  $\pm 3\%$ .

The second approach for proving the quality of closure of the moisture balance is an integral method. Here, a certain amount of liquid is sprayed onto pre-dried particles so that the particle moisture content increases. After a certain time the

**Tab. 1.4** Maximal deviation of differential balance.

$\dot{M}_l \text{ [mg s}^{-1}\text{]}$	$\Delta \dot{M}_v \text{ [mg s}^{-1}\text{]}$	Error [%]
82.08	$\pm 2$	$\pm 2.43$
110.64	$\pm 2$	$\pm 1.80$
134.23	+4	+2.97

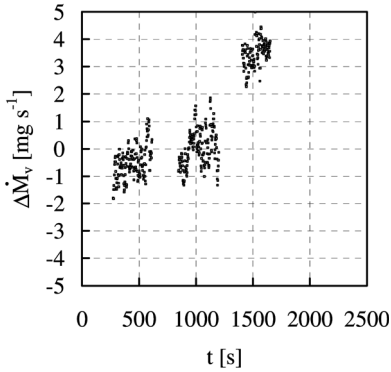


Fig. 1.15 Calculated deviation of differential moisture balance.

spraying is shut down and the moisture is removed again from the particles. Gas outlet humidity is detected during the entire process. By integral evaluation of these signals the total amount of evaporated water can easily be quantified:

$$M_v(t) = \int \dot{M}_g(Y_{out} - Y_{in})dt \quad (1.9)$$

For these trials the same test material was utilized as in the previous experiments. The spraying rate was adjusted to  $0.13 \text{ g s}^{-1}$ . Results for two gas flow rates of  $50.66$  and  $30.15 \text{ kg h}^{-1}$  are presented in Fig. 1.16 and Fig. 1.17, respectively. Diagram (a) depicts in each case the temporal change of gas moisture content while diagram (b) illustrates the deviation of integral moisture balance obtained from

$$\Delta M_v = M_l(t) - M_v(t) \quad (1.10)$$

The evolution of gas moisture content reflects clearly the pre-drying, the spraying and the drying periods. Since the gas mass flow rate was reduced for the second trial,

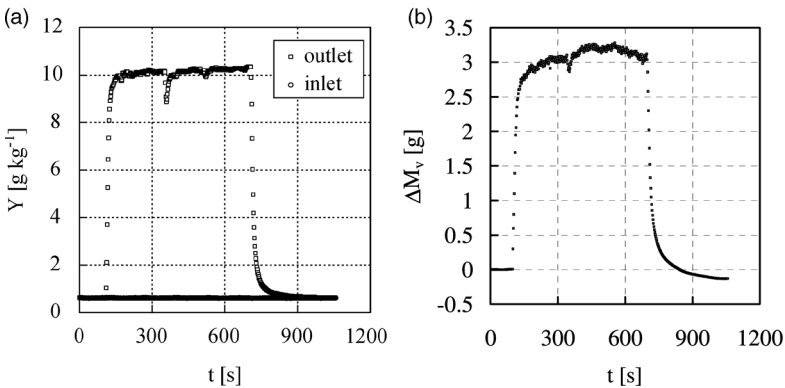
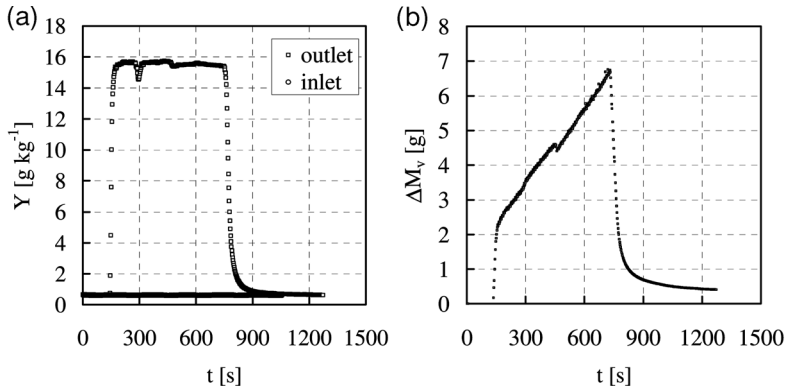


Fig. 1.16 Experimental results for proving the integral water balance at a gas mass flow rate of  $50.66 \text{ kg h}^{-1}$ ; (a) temporal change of gas moisture content; (b) deviation of cumulative mass of water.



**Fig. 1.17** Experimental results for proving the integral water balance at a gas mass flow rate of  $30.15 \text{ kg h}^{-1}$ ; (a) temporal change of gas moisture content; (b) deviation of cumulative mass of water.

**Tab. 1.5** Final deviation of integral balance.

Exp.	$\dot{M}_g \text{ [kg h}^{-1}\text{]}$	$M_l \text{ [g]}$	$M_v \text{ [mg s}^{-1}\text{]}$	Error [%]
1	50.66	82.026	82.156	-0.16
2	30.15	81.627	81.219	+0.50

the gas outlet humidity reaches significantly higher values of about  $16 \text{ g kg}^{-1}$ . The initial increase in the deviation of moisture balances indicates the accumulation of water in the bed material. Actually, this value can be directly converted into a moisture content of particles if the dry solids mass is known. The second experiment shows a similar behavior of gas humidity, but a different evolution of  $\Delta M_v$ . The temporal change in this value indicates that the accumulation of water in the particles increases continuously, even at constant gas outlet moisture. At the end of the experiments – after the drying period – the value of  $\Delta M_v$  should return to zero. This would mean that we have found in the gas outlet all the water that we have sprayed into the bed and would, thus, correspond to perfect closure of the integral moisture balance. The measured final values of  $\Delta M_v$  are summarized in Tab. 1.5. They show that the error of the integral moisture balance is less than 1% for both cases, which is a very nice validation for the accuracy of the experimental set-up and the instrumentation.

### 1.3.6

#### A Case Study: Determination of Single Particle Drying Kinetics of Powdery Material

After successful validation of the instrumentation and the experimental set-up, derivation of fluidized bed drying curves from outlet gas humidity measured by IR spectroscopy will be illustrated. As already discussed, such fluidized bed drying curves can be used – in a second step – to derive single particle drying kinetics of

Tab. 1.6 Parameters of fluidized bed drying experiments.

Exp	$T_g$ [°C]	$M_{0,wet}$ [g]	$X_0$ [kg kg <sup>-1</sup> ]	$\dot{M}_g$ [kg h <sup>-1</sup> ]	$Y_{in}$ [g kg <sup>-1</sup> ]
1	50	200.23	0.1788	21.37	0.66
2	50	200.52	0.1786	20.56	0.66
3	40	200.25	0.1874	21.31	0.65
4	60	200.45	0.1854	20.79	0.65

powdery materials, which is not accessible directly because of their too small particle diameter.

To this purpose, drying experiments were conducted with powdery polymer (particle diameter:  $d = 168 \mu\text{m}$ , dry particle density:  $\rho_p = 1123 \text{ kg m}^{-3}$ ). All experiments were carried out under approximately the same process conditions with respect to the mass flow rate of fluidization gas, initial bed mass and gas inlet moisture content. Operating parameters are summarized in Tab. 1.6.

Figure 1.18 shows a typical result for the temporal change of moisture content during the drying process. After feeding the wet batch into the apparatus the gas outlet moisture changes rapidly while the inlet moisture (both measured by IR spectroscopy) remains constant throughout the entire experiment. Initially, the outlet moisture exceeds somewhat the theoretical maximum of adiabatic saturation moisture. This phenomenon is caused by the thermal capacity of the apparatus, mainly the air distributor, and the bed material. After a relatively short period the outlet moisture starts to decrease towards the value of the inlet. From this data the temporal change of particle moisture content can directly be withdrawn, taking into account the initial moisture of particles  $X_0$ . The value of  $X_0$  was determined by drying a sample of approximately 40 g in a vacuum oven at 80 °C for 24 h. Additional measurement of the final moisture content of the solids enables one to check the closure of water mass balance.

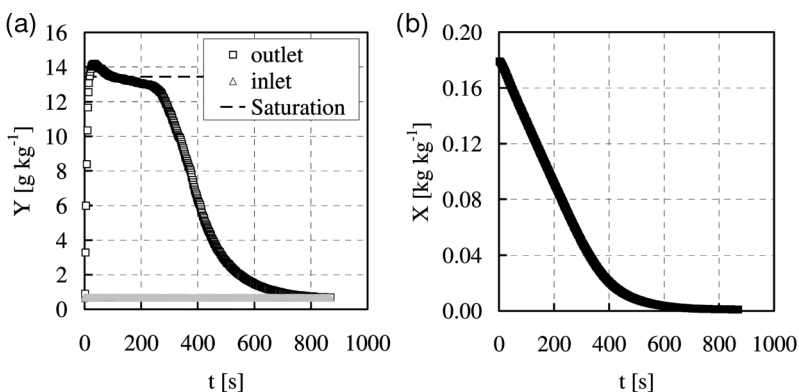


Fig. 1.18 Typical measurement results of drying in a batch fluidized bed (Exp. 1 from Tab. 1.6); (a) outlet gas humidity; (b) solids moisture content.

A better way of presenting the results is to use, instead of the plot of Fig. 1.18b, the drying curve, where the drying rate

$$\dot{m}_v = \frac{\dot{M}_g(Y_{out} - Y_{in})}{A_{bed}} \quad (1.11)$$

that refers to the total surface area of the particles is plotted vs. the particle moisture content. Such a diagram is shown in Fig. 1.19a. Direct comparison between drying processes conducted under different process conditions is easier in terms of drying curves because time has been eliminated. To check the reproducibility of results, drying at 50 °C was repeated twice. Direct comparison of the data in Fig. 1.19a shows a very good agreement between the two trials throughout the entire experiment. This is additional proof of the reliability of the method.

As mentioned above, measurements in a fluid bed dryer do not represent single particle behavior but can be used to scale down to the single particle level by applying an adequate model. In this study, the fluidized bed drying model introduced by Groenewold and Tsotsas (1997) – see also Burgschweiger and Tsotsas (2002), Groenewold and Tsotsas (2007) – has been employed. The model distinguishes between bubble phase and suspension phase. All parameters such as bypass ratio, Sherwood number from particle to suspension phase, and number of transfer units from suspension to bubble phase are set. The only degree of freedom concerns single-particle drying kinetics in the form of a normalized drying curve. This curve is fitted to fluidized bed drying data in the course of scale down. In calculations of fluidized bed drying at conditions other than those used for fitting, single particle drying behavior is an input, so the model works in a fully predictive mode.

The inhibition of the drying rate of particles at low moisture contents in terms of single particle drying kinetics can be considered in different ways. One possible approach is normalization in order to describe measured drying curves by reduction to just one normalized (or characteristic) drying curve for the considered product.

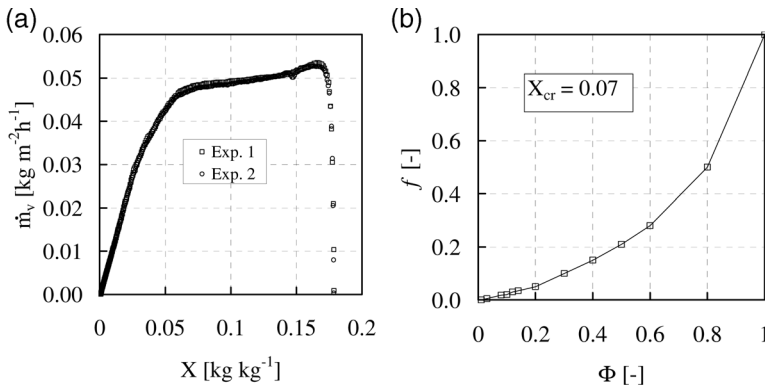


**Fig. 1.19** (a) Reproducibility of drying curves measured in a batch fluidized bed; (b) normalized single particle drying curve and critical moisture content derived from Exp. 1 (Tab. 1.6) by application of a fluid bed drying model.

This method was introduced for normalization of drying curves measured in batch drying by van Meel (1958), and since then it has been applied in the original or in modified forms by many authors (van Brakel, 1980; Shibata, 2005; Groenewold, 2004). The normalized drying rate  $f$  is defined as the quotient of the actual drying rate  $\dot{m}_v$ , and the drying rate of the first drying period  $\dot{m}_{v,1}$

$$f = \frac{\dot{m}_v}{\dot{m}_{v,1}} \quad (1.12)$$

and the normalized solids moisture content,  $\Phi$ , is represented by

$$\Phi = \frac{X - X_{eq}}{X_{cr} - X_{eq}} \quad (1.13)$$

where  $X_{eq}$  is the equilibrium moisture content. Both  $f$  and  $\Phi$  take values between 0 and 1.

Remember that drying is assumed to be gas-side controlled in the first and particle-side controlled in the second drying period (at  $X < X_{cr}$ ). By normalization the two periods are separated from each other. Gas-side phenomena (i.e. the drying rate  $\dot{m}_{v,1}$ ) are supposed to be predictable from first principles. Particle-side phenomena are described empirically by the function  $f(\Phi)$ . Successful normalization leads to a function  $f(\Phi)$  which is invariant with drying conditions (Tsotsas, 1994; Suherman *et al.*, 2008).

Applying this concept, the normalized drying curve of a single particle as well as the critical moisture content are derived by scaling down from measurement results by iterative adjustment in a computer program that implements the fluidized bed drying model. For this derivation the data from experiment 1 (Tab. 1.6) has been used. The normalized drying curve is presented graphically in Fig. 1.19b, with a critical moisture content of  $X_{cr} = 0.07$  for this product.

Figure 1.20 illustrates the opposite exercise, by comparing calculations conducted with the normalized drying curve that has been derived from one experiment with the

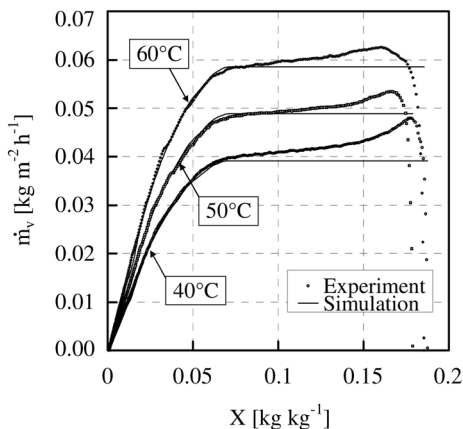


**Fig. 1.20** Comparison between measured and calculated fluidized bed drying curves at different temperatures.

results of three fluidized bed experiments carried out at different gas inlet temperatures. The results show that at high moisture content the measured drying rate is higher than the calculated one. As mentioned above, this is a thermal effect mainly caused by the supply of heat to the fluidized bed from the equipment, in particular from the distributor plate. Before every drying experiment, the entire apparatus is warmed to the inlet gas temperature. After the start of the experiment, heat transfer takes place between the equipment and the drying gas and/or the equipment and the particles, since both the average gas temperature and the particle temperature are clearly lower than the gas inlet temperature in the first drying period. As a result of this additional energy, drying rates increase. Towards the end of the drying process, the drying rate reaches very small values, which are still determined from the difference between the outlet and inlet gas humidities. Since the respective measured quantities become almost identical and exhibit a certain noise, scatter of the drying rates is unavoidable at low moisture contents. Nevertheless, the derivation of drying rates appears to be accurate enough till solids moisture contents of about 0.002 in the present experiments.

In spite of such restrictions, Fig. 1.20 shows quite good agreement between measurement and simulation in the significant range of moisture content. This is true, in particular, for the influence of temperature. Consequently, the concept of normalization works well for the present example. This is not always the case (Suherman *et al.*, 2008), so that it may be better to use, for example, some diffusion model instead of the normalization method for other products. Then, diffusion coefficients will be the quantities to determine by fitting of the fluidized bed drying model to the experimental results. Apart from this, the described procedure remains essentially the same.

## 1.4 Coulometry and Nuclear Magnetic Resonance

### 1.4.1 Particle Moisture as a Distributed Property

In this section, we address the problem of measuring the relatively low moisture content of a large number of particles on an individual basis with the necessary precision. This problem arises when particulate material is dried and particle moisture at the outlet of the dryer is not uniform. In such a case, the characteristics of the distribution of particle moisture decide the quality of the drying process. In general, the outlet moisture content of any product must be below some specified value for quality reasons, but over-drying is undesirable because of energy costs, capacity restrictions or product damage. In the following, we choose the example of a continuous fluidized bed dryer (as sketched in Fig. 1.21) to illustrate, first, how the moisture content distribution may be approximated by a simplified population balance model and, then, how it can be measured. Subsequently, measured moisture distributions will be compared with the model.

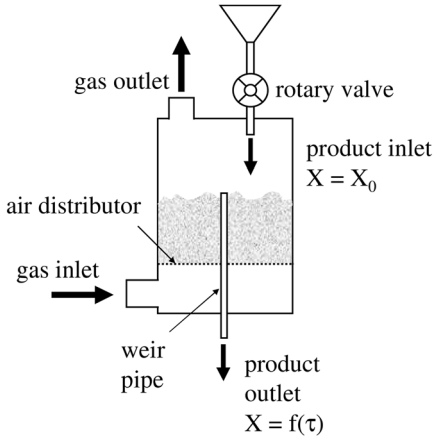


Fig. 1.21 Scheme of continuous fluidized bed dryer.

#### 1.4.2

### Modeling the Distribution of Solids Moisture at the Outlet of a Continuous Fluidized Bed Dryer

The objective of the present approach is to provide an analytical solution for distributed moisture content of particles at the dryer outlet. To this purpose, we take a certain functional form of the normalized drying curve, Eq. 1.14, and, in contrast to previous studies (Burgschweiger and Tsotsas, 2002; Kettner *et al.*, 2006), do not include energy balances for the solid phase or any balances for the gas phase. Particles (of uniform diameter  $d_p$  and density  $\rho_p$ ) are conveyed into the dryer at a constant particle flow rate  $\dot{N}_0$ , all having the same initial moisture content  $X_0$ . Discharge of particles is by an internal weir pipe, the height of which controls the total hold up of solids ( $N_{\text{bed}}$  particles). Furthermore, the dryer is assumed to be sufficiently small so that the spatial distribution of solids has no influence. In this case, particles with the same residence time  $\tau$  also have the same moisture content  $X(\tau)$  and the residence time distribution of the particles in the dryer (corresponding to that of a continuous stirred tank reactor) is the only reason for a distribution of moisture content.

For the drying kinetics of a single particle, we assume the functional form of the normalized drying rate

$$f = \frac{\dot{m}_v}{\dot{m}_{v,1}} = \begin{cases} 1 & \text{for } \Phi \geq 1 \\ \frac{p\Phi}{1 + \Phi(p-1)} & \text{for } \Phi < 1 \end{cases} \quad (1.14)$$

where  $p$  is an adjustable parameter,  $\dot{m}_v$  is the particle drying rate and

$$\dot{m}_{v,1} = \rho_g \beta (Y_{\text{as}} - Y) \quad (1.15)$$

is the rate of the first drying period ( $\rho_g$ : dry gas density,  $\beta$ : gas-side mass transfer coefficient,  $Y_{\text{as}}$ : adiabatic saturation moisture,  $Y$ : moisture content in the bulk of the

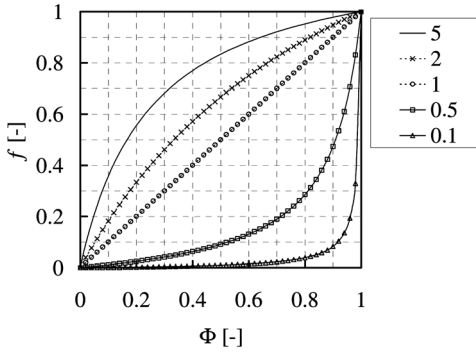


Fig. 1.22 Influence of parameter  $p$  on normalized drying curve of single particle.

gas). The dimensionless moisture content  $\Phi$  is defined according to Eq. 1.13. Figure 1.22 illustrates how this function, which is the same as the function for ideal liquid–vapor equilibrium in distillation, can describe a wide range of drying curves by variation of parameter  $p$ .

For such conditions, the following analytical expression can be derived for the cumulative number distribution of particle moisture at the outlet of the dryer:

$$N(X) = \begin{cases} N_{\text{bed}} \exp\left(-\frac{X_0 - X}{K\bar{\tau}}\right) & \text{for } X \geq X_{\text{cr}} \\ N_{\text{bed}} \exp\left(-\frac{\tau_{\text{cr}}}{\bar{\tau}}\right) \cdot \exp\left(\frac{p-1}{Kp\bar{\tau}}(X - X_{\text{cr}})\right) \cdot \left(\frac{X - X_{\text{eq}}}{X_{\text{cr}} - X_{\text{eq}}}\right)^{\frac{X_{\text{cr}} - X_{\text{eq}}}{Kp\bar{\tau}}} & \text{for } X < X_{\text{cr}} \end{cases} \quad (1.16)$$

Equation 1.16 contains three characteristic dimensionless quantities, the rate constant

$$K = \frac{6 \cdot \rho_g \cdot \beta}{\rho_p \cdot d_p} (Y_{\text{as}} - Y) \quad (1.17)$$

the mean residence time

$$\bar{\tau} = \frac{N_{\text{bed}}}{\dot{N}_0} \quad (1.18)$$

and the critical time

$$\tau_{\text{cr}} = \frac{X_0 - X_{\text{cr}}}{K} \quad (1.19)$$

Typical results are plotted as normalized distributions  $Q_0 = N/N_{\text{bed}}$  in Fig. 1.23 for the operating parameters given in Tab. 1.7 and different single particle drying curves (by variation of  $p$ ). For particle moistures  $X > X_{\text{cr}}$ , the curves are identical, since the drying rate of the first drying period is independent of  $p$ . In the second drying period, however, the distributions differ significantly. A decrease in the value of  $p$ , which corresponds to a decrease in drying rate, shifts the distribution to

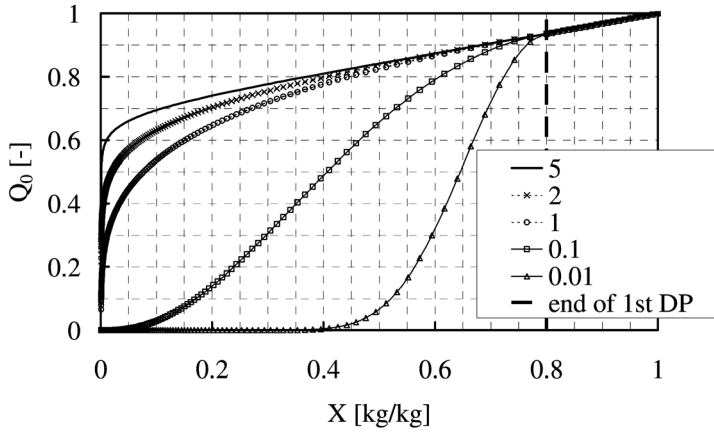


**Fig. 1.23** Normalized cumulative number distributions of particle moisture for different values of parameter  $p$  (remaining parameters according to Tab. 1.7).

higher moisture contents. Moreover, the width and shape of the distribution are also strongly affected.

### 1.4.3

#### Challenges in Validating the Model

In the experiments for testing the above model,  $\gamma\text{-Al}_2\text{O}_3$  beads with Sauter diameter  $d_p = 1.8\text{ mm}$  and particle density  $\rho_p = 1040\text{ kg m}^{-3}$  are used. Since the initial moisture content of these particles is around 0.65, the water contained in a single particle is at most around 2 mg. After drying, most of this moisture will have been removed so that we need a method to detect amounts of water in the range of a few hundred  $\mu\text{g}$  with good precision. Gravimetric methods have here reached their limit: the relatively high dry particle mass of 3.2 mg and strong hygroscopic behavior of the

**Tab. 1.7** Parameter settings for the curves of Fig. 1.23.

Parameter	Symbol	Value	Unit
Mass of bed material (dry)	$M_{\text{bed}}$	1	kg
Particle flow rate (dry)	$\dot{M}_p$	2	$\text{g s}^{-1}$
Particle diameter	$d_p$	1	mm
Particle density (dry)	$\rho_p$	1000	$\text{kg m}^{-3}$
Gas density (dry)	$\rho_g$	1	$\text{kg m}^{-3}$
Mass transfer coefficient	$\beta$	0.05	$\text{m s}^{-1}$
Saturation moisture	$Y_{\text{as}}$	21	$\text{g kg}^{-1}$
Moisture in gas bulk	$Y$	1	$\text{g kg}^{-1}$
Initial particle moisture	$X_0$	1	$\text{kg kg}^{-1}$
Critical moisture	$X_{\text{cr}}$	0.8	$\text{kg kg}^{-1}$
Equilibrium moisture	$X_{\text{eq}}$	0.001	$\text{kg kg}^{-1}$

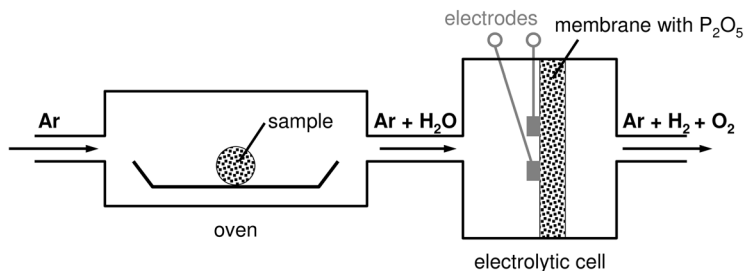


**Fig. 1.24** Measurement principle of coulometer for detecting water in solid samples.

material (leading to significant moisture uptake during weighing) prevent an accurate measurement of moisture content.

When searching for an appropriate measurement method, we also have to bear in mind that a sufficient number of particles (at least 100) have to be characterized for a reliable comparison of experimental and theoretical distribution functions.

In the following, we present the methods of coulometry and nuclear magnetic resonance; we will see, by analysis of their advantages and disadvantages, that a combination of both techniques is suitable for fast and accurate moisture measurements.

#### 1.4.4

#### Coulometry

The principle of coulometry is to determine the quantity of a species by measuring the electric charge  $Q$  (in Coulomb) required to completely decompose this species by a well-known electrolytic reaction. Since small electric currents can easily be controlled, measured and integrated over time, the method is suitable for detecting very small species quantities. For example, an electrolysis current of 1 mA reduces water into hydrogen and oxygen at a rate of merely  $0.0933 \mu\text{g s}^{-1}$ . The first electrolytic cell to continuously measure small amounts of water in gas flows was proposed by Keidel (1959) who already anticipated a wide range of applications to liquids and solids if water is transferred into a gas stream by controlled evaporation at low rates. The water detection system which is discussed in the following, namely WDS 400 by Sartorius, is very similar to this first device; its major components are sketched in Fig. 1.24.

The wet solid sample is put into an oven (see also Fig. 1.25b) which may be heated to a temperature of  $400^\circ\text{C}$  according to a pre-set temperature protocol. The oven is continuously swept by a dry inert or noble gas at a constant flow rate of  $100 \text{ ml min}^{-1}$  taking up the evaporated water (and possibly other volatile substances). The gas mixture flows through a ceramic membrane that serves as a carrier for phosphorus pentoxide  $\text{P}_2\text{O}_5$ . Due to the extreme hygroscopicity of this substance, all water vapor is absorbed and phosphorus pentoxide is converted (in several hydration steps) to orthophosphoric acid



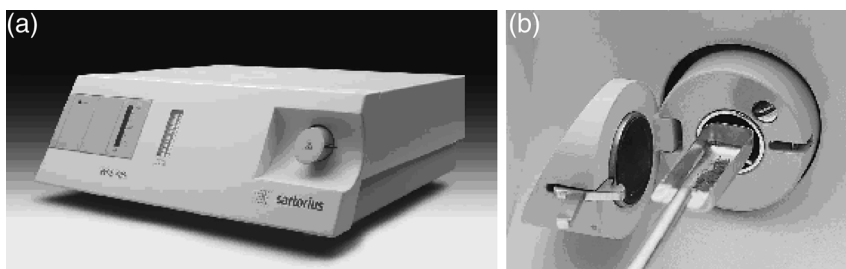


**Fig. 1.25** Desktop coulometer (a) with oven (b) into which a powder sample is loaded (by courtesy of Sartorius Co.).

Gas components other than water will pass through the membrane without reaction. Voltage is applied to the membrane by two electrodes (printed on its surface) to dissociate the phosphoric acids, the final step of the respective anodic and cathodic reactions being

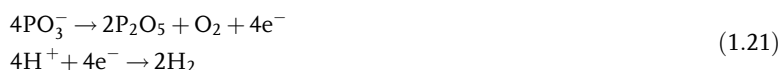
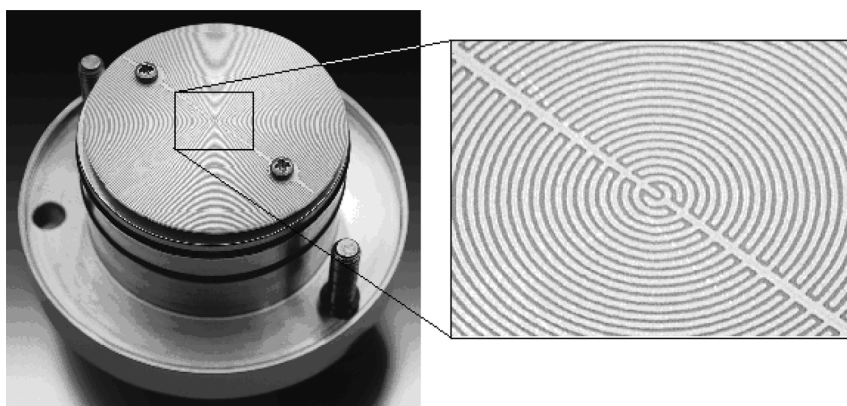


Figure 1.26 shows the electrodes on the membrane which have a strongly interlaced geometry to get a large active area and short paths for the electrolytic reaction. The electric current through the electrolytic cell is measured as a function of time; integration yields the total electric charge consumed by electrolysis, which may be directly converted into a mass of water. Since hydrolysis and electrolytic recovery of phosphorus pentoxide are simultaneous reactions, care must be taken that the cell does not get saturated with water. To this purpose, a maximum electrolytic current (for the given device 100 mA) must not be exceeded, that is



**Fig. 1.26** Electrolytic cell with magnification of the two interlaced electrodes (light gray) that are printed on the membrane (dark gray) (by courtesy of Sartorius Co.).

water vapor must not be produced in the oven at too high rates (at a maximum  $9.3 \mu\text{g s}^{-1}$ ). On the other hand, too low electrolytic currents – associated with too low evaporation rates – will be measured with a higher relative error so that water content is obtained at lower precision (integration over time has no effect on the error). In conclusion, best results are obtained for elevated but not too high evaporation rates (here several  $\mu\text{g s}^{-1}$ ).

It should be noted that the value of the electrolytic voltage is not critical as long as it is well above 2 V, which is the decomposition voltage of water (Keidel, 1959).

The efficiency of the cell depends on impurities and is regularly assessed by calibration measurements with a well-defined amount of water. Since free water would evaporate too rapidly and lead to an overload of the detector, a standard substance, sodium wolframate containing crystalline water ( $\text{Na}_2\text{WO}_4 \cdot 2\text{H}_2\text{O}$ ), is used; typically, 20–25 mg of standard substance (with 1.07% water) are used. If the efficiency is too low, the electrolytic cell has to be refreshed by cleaning with water and coating with an acetone solution of 85% orthophosphoric acid ( $\text{H}_3\text{PO}_4$ ). Before performing the next analysis measurement, the cell must be dried and the acid converted into phosphorus pentoxide by electrolysis. The dehydration will, however, not be complete ( $\text{HPO}_3$  is considered the prevailing component) since the cell becomes an insulator with increasing concentrations of  $\text{P}_2\text{O}_5$  (Keidel, 1959).

For quantitative analysis of water in solid samples, the following procedure is applied:

1. Open the oven door and insert the sample scoop
2. Close the oven door (a short time interval later)
3. Heat the oven according to a pre-set temperature protocol
4. Measure and integrate the electrolysis current over a given time interval.

It is obvious that such a measurement will not only detect the water from the sample, but also residual moisture in the flow of carrier gas and moisture that enters the system when opening the oven door; (recall that saturated air at  $20^\circ\text{C}$  contains  $17.3 \mu\text{g ml}^{-1}$  water vapor and the total oven volume is 26 ml). From this, it is obvious that tare measurements without a solid sample are of paramount importance if small solids moisture contents are to be quantified. Such a tare measurement has to be done directly before quantitative analysis to account for changes of relative humidity in ambient air; furthermore, exactly the same procedure has to be respected as in the subsequent analytic measurements, that is same open time of oven, same temperature protocol and measurement duration.

We will now return to our task of characterizing particles from a fluidized bed dryer with respect to their moisture content, which corresponds to measuring water amounts in the range 100–2500  $\mu\text{g}$ . Recalling that the temperature protocol ideally has to be chosen so as to evaporate water from the sample at a rate of several  $\mu\text{g s}^{-1}$ , we will apply two different protocols. The first, which is applied to particles with rather low moisture, accomplishes a temperature increase to  $130^\circ\text{C}$  in one step and in total takes 10 min (see Fig. 1.27a). The second is intended for larger amounts of water; in order to prevent too high release rates, an intermediate temperature of  $60^\circ\text{C}$  is first assumed before heating to  $130^\circ\text{C}$  in a second step; overall measurement duration is

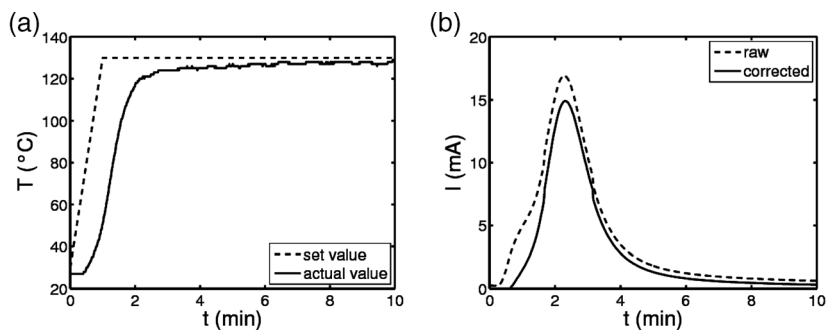


**Fig. 1.27** (a) Temperature protocol and (b) electrolysis current for a particle with low moisture content ( $M_w = 161 \mu\text{g}$ , sample A).

14 min (see Fig. 1.28a). To obtain reproducible results, argon (99.998 vol.%) at a flow rate of approximately  $100 \text{ ml min}^{-1}$  is used as a dry carrier gas in all measurements.

Tare measurements of electrolysis current for the two chosen temperature protocols are given in Fig. 1.29. One may assume a constant background level that originates from residual moisture in argon (a gas flow of  $100 \text{ ml min}^{-1}$  with 0.002 vol.% water vapor corresponds to a vapor flow of  $1.48 \mu\text{g min}^{-1}$  or an electric current of 0.26 mA). The different durations of the two protocols result in different contributions from argon to the total detected moisture (14.8 and  $20.7 \mu\text{g}$  for protocols 1 and 2, respectively).

The signal above this background results from the moisture entering the oven during (sample) loading. Its shape depends slightly on the chosen temperature protocol but not its integral value (39.8 and  $39.5 \mu\text{g}$  for protocols 1 and 2, respectively). In this light, we may understand the detection limit of the device that is given as  $1 \mu\text{g}$ .

In the following, five samples (A–E) with increasing moisture content are characterized. The complete measurement results are given for the driest and for the wettest sample in Figs. 1.27 and 1.28, respectively. In Figs. 1.27a and 1.28a the oven temperature is plotted along with the value set by the protocol. Figures 1.27b and 1.28b show the electrolysis current which is corrected by the tare measurement.

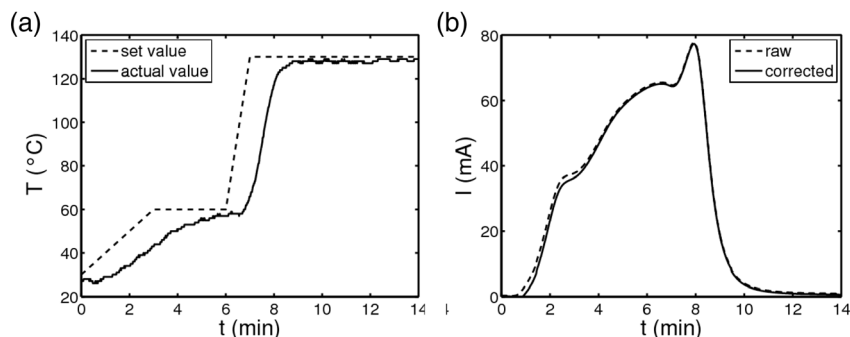


**Fig. 1.28** (a) Temperature protocol and (b) electrolysis current for a particle with high moisture content ( $M_w = 2171 \mu\text{g}$ , sample E).

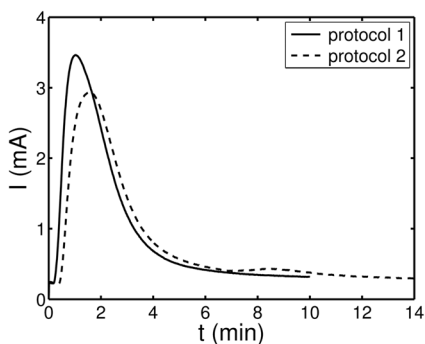


**Fig. 1.29** Tare measurements for the two temperature protocols shown in Figs. 1.27 and 1.28; the converted electric charge is equivalent to  $54.6\ \mu\text{g}$  (protocol 1) and  $60.2\ \mu\text{g}$  (protocol 2) of water.

Figure 1.30 summarizes the corrected electrolysis currents and computed water amounts for all five samples. Having seen that the coulometric method can produce quantitative results of the desired high quality, we conclude our description by recalling its major advantages and disadvantages. The major advantages may be listed as:

- In the coulometric method, water is clearly distinguished by a chemical reaction, whereas in gravimetric methods, for example the magnetic suspension balance, weight loss during heating is recorded and the assumption must be made that water loss is the only reason for the weight change. In reality, however, elevated temperatures may also lead to weight loss by chemical reactions in the solid or evaporation of volatile substances.
- The mass of water  $M_w$  is measured directly so that only the wet sample  $M_{s,\text{wet}}$  (original state) needs to be weighed to obtain the moisture content from  $X = M_w / (M_{s,\text{wet}} - M_w)$ . In gravimetric methods, the dry solid mass  $M_{s,\text{dry}}$  must also be

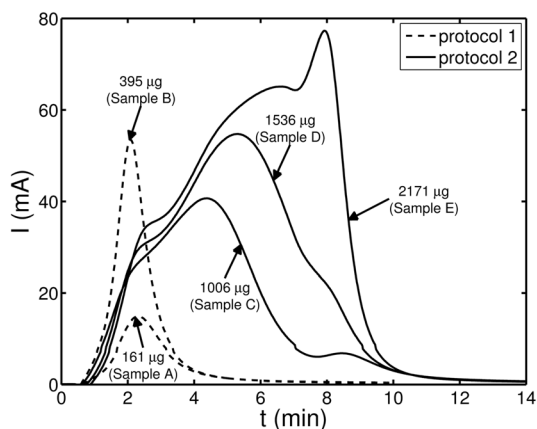


**Fig. 1.30** Electrolysis current for five particles spanning a wide range of moisture content.

measured to compute the moisture content as  $X = (M_{s,\text{wet}} - M_{s,\text{dry}})/M_{s,\text{dry}}$ . This brings the problem of removing all water without any other changes to the sample. Furthermore, in the case of low moisture contents, the weight difference  $M_{s,\text{wet}} - M_{s,\text{dry}}$  cannot be measured accurately due to limited balance precision, and this may reflect in a large error in  $X$ .

- The coulometric method may also be used for a rough quantitative distinction of surface water, capillary water and the more tightly bound water of crystallization if the temperature rise is performed in appropriate steps.

The major disadvantages of the coulometric method are:

- The sample as defined by a porous structure containing a certain amount of water is destroyed so that the measurement cannot be repeated.
- Sample water content and release behavior of the water must be known approximately so as to choose the optimal temperature protocol: on the one hand, the electrolytic cell must not get saturated; on the other hand, the release rate should not be too low so as to keep the measurement period short (see above). When looking at the stochastic behavior of particles in a continuous fluidized bed dryer, such information is not available!
- The measurement of one sample takes a relatively long time (about 20 min). If many samples need to be measured to describe stochastic behavior, this is a severe drawback.
- The humidity of a relatively big gas volume (oven) needs to be corrected in a tare measurement.

#### 1.4.5

#### **Nuclear Magnetic Resonance**

An alternative method to measure the amount of water contained in a wet sample uses the magnetic spin of its hydrogen nuclei  $^1\text{H}$  (protons, compare with Chapter 4). If protons are put in a magnetic field, their magnetic moments will behave according to quantum mechanical rules and take one of two stationary states: parallel or anti-parallel to the external magnetic field  $B_0$ . The parallel state is thermodynamically favorable so that a macroscopic magnetization  $M$  is observed, which is proportional to the number of protons; it increases with magnetic field strength and decreases with temperature according to Boltzmann's law. In the unperturbed state, magnetization  $M$  stays aligned with the magnetic field  $B_0$ . However, if the two are *not* parallel, magnetization will rotate around the magnetic field vector with nuclear magnetic resonance frequency  $\omega_0$ , as shown in Fig. 1.31, and produce an electromagnetic signal that can be measured. The NMR frequency depends on the nucleus and on the magnetic field  $B_0$ ; for protons, a magnetic field of 7T produces a frequency of about 300 MHz.

In order to get the magnetization vector  $M$  tilted with respect to  $B_0$ , a small additional magnetic field  $B_1$  is applied which rotates in the  $x$ - $y$ -plane with NMR

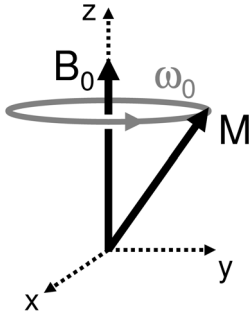


Fig. 1.31 Precession of magnetization  $M$  in an external magnetic field  $B_0$ .

frequency  $\omega_0$ . By adjusting the magnitude of  $B_1$  and the pulse duration, the flipping angle can be tuned to  $90^\circ$ , which will produce the highest resonance signal. In practice, the same electromagnetic coil first produces the rotating  $B_1$ -field and then (after a short dead time) measures the signal of the rotating  $M$ -vector. This NMR signal decays with the so-called transverse relaxation time  $T_2$  because the rotating protons get out of phase due to small variations of NMR frequency in time and space; in consequence, the component of  $M$  orthogonal to the  $z$ -axis becomes zero. On a longer time scale (characterized by longitudinal relaxation time  $T_1$ ), the magnetization will relax back to its equilibrium state, that is parallel to  $B_0$ .

This type of NMR measurement is referred to as free induction decay (FID) because the protons may relax after the initial pulse without further perturbation. The initial magnitude of the FID signal is proportional to the number of protons. However, the signal of adsorbed water decays faster than that of free water because of its strong interaction with the solid (Metzger *et al.*, 2005). This is one reason why the overall signal does not decay exponentially.

Experiments on the wet  $\gamma\text{-Al}_2\text{O}_3$  samples were performed in a Bruker Avance 300 MHz NMR spectrometer (see Fig. 1.32) with micro-imaging option. The sample was put in an NMR glass tube and set into the 5 mm resonance coil in a central position (see Fig. 1.33a). To insert the glass tube into the narrow opening, a conical Teflon guide was put on top of the resonance coil (see Fig. 1.33b). Free induction signals are plotted in arbitrary units in Fig. 1.34 for the five samples that have also been characterized by coulometry (see above). Additionally, the NMR signal for an empty tube (i.e. without sample) is shown as a dashed line. For good signal-to-noise ratio, 100 scans were added together with a time delay of 1 s to assure longitudinal relaxation.

The magnification of the very first data points (Fig. 1.34a) shows an initial contribution to the signal that is independent of the sample (dashed line) and decays in about  $40\ \mu\text{s}$ ; it probably results from the resonance coil itself. The semi-logarithmic plot of the NMR signal (Fig. 1.34b) confirms shorter decay times for relatively dry samples where adsorbed water is dominant; it also reveals that decay is not strictly exponential.

On the basis of these findings it has been decided that the first data points have to be discarded and that the initial signal amplitude is not estimated by an exponential

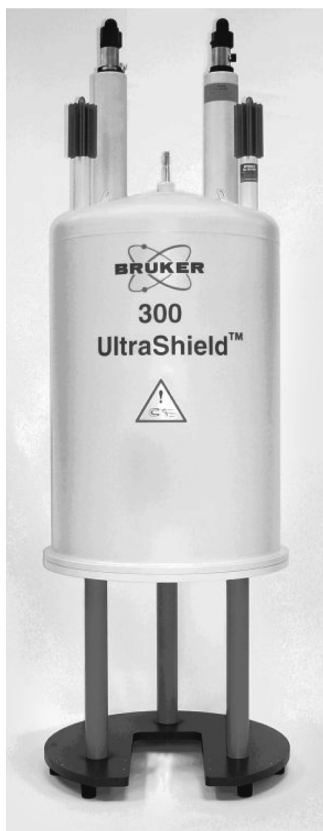
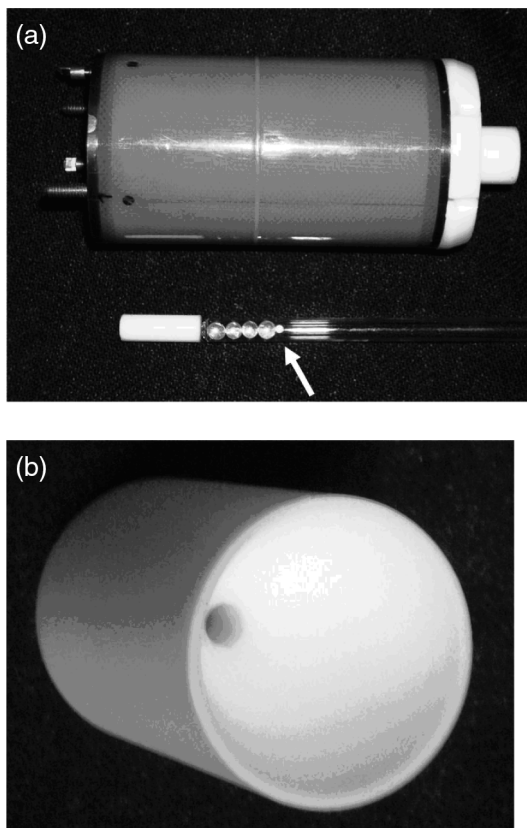


Fig. 1.32 Bruker Avance 300 MHz NMR spectrometer (courtesy of Bruker Biospin Co.).

fit but instead approximated by the first reasonable value (measured after  $34.5 \mu\text{s}$ ). The reproducibility of these values was found to be around 1%.

Summarizing the advantages of the described NMR method we may state that, in contrast to the method of coulometry:

- No approximate knowledge is needed about the moisture content of the sample because the same measurement protocol is applied to wet and dry samples.
- The wet sample is not “destroyed” so the measurement may be repeated.
- Experimental time can be made short, depending on the desired accuracy (100 s for the chosen protocol).
- The measured particle moisture is affected by the gas in the test tube (about  $2 \text{ cm}^3$ ) only because of sampling – establishing new sorption equilibrium – and not because of the measurement method itself (cf. opening of oven door in coulometry). The resulting error may be reduced by filling the empty part of the tube with inert material.



**Fig. 1.33** (a) NMR resonance coil and sample (arrow) in glass tube with Teflon cylinder and glass spheres to achieve a central position; (b) Teflon cone to guide tube into coil.

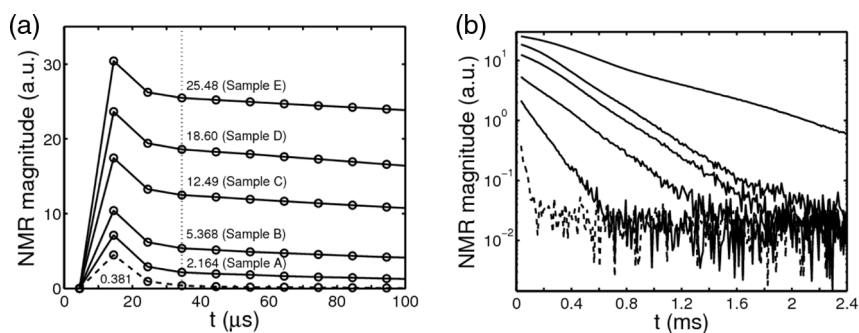


**Fig. 1.34** Free induction decay for five samples and empty tube (a) first ten data points and (b) decay behavior over a longer period of time (semi-logarithmic plot).

The major disadvantages of the proposed NMR method are:

- The need for calibration. Ideally, the signal is proportional to the mass of water  $M_w$  so that only one point would be required. Unfortunately, we will see that strict proportionality is not observed and that a calibration *curve* is needed instead.
- The high cost of the system, also in terms of operation and maintenance (especially the need for liquid helium and nitrogen to cool the superconducting magnet).

However, NMR devices can be found in all major research institutions because of their wide range of scientific applications. And the problem of calibration may be solved by combining the method with precise coulometric experiments.

#### 1.4.6

##### Combination of Both Methods

In Figure 1.35, the NMR signals of the five selected samples are plotted versus the mass of water which has been measured (afterwards) by the method of coulometry. The non-zero signal of the empty tube is also shown. From the data points it becomes clear that one-point calibration (assuming proportionality) is not reasonable; furthermore, the comparison between linear and quadratic fit reveals that the correlation is not strictly linear so that a quadratic calibration curve is chosen. Several additional data sets (not shown here) could confirm the accuracy of the calibration curve.

With this newly developed method, we will now measure distributions of particle moisture.

#### 1.4.7

##### Experimental Moisture Distributions and Assessment of Model

The experiments for testing the model from Section 1.4.2 are carried out in a continuous laboratory scale dryer as depicted in Fig. 1.21, with a diameter of 150 mm

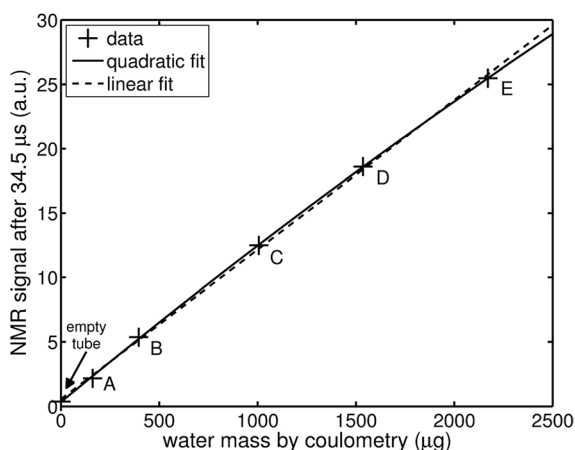


Fig. 1.35 Calibration of NMR signal by coulometry.

Tab. 1.8 Experimental and simulation parameters for particle flow rate variation.

Symbol	Exp. 1	Exp. 2	Exp. 3	Unit
$M_{bed}$	0.982	0.820	0.976	kg
$\dot{M}_p$	1.7	1.3	1	$\text{g s}^{-1}$
$Y$	17.39	13.78	11.67	$\text{g kg}^{-1}$
$X_{eq}$	0.09	0.08	0.06	$\text{kg kg}^{-1}$
$K$	$1.12 \times 10^{-3}$	$1.96 \times 10^{-3}$	$2.37 \times 10^{-3}$	$\text{s}^{-1}$

and a batch size of approximately 3 l. The instrumentation provides various measurements of temperature, pressure, pressure difference, gas flow rate, and inlet and outlet gas moisture.

Three experiments were run with different particle flow rates, but the same inlet solids moisture content ( $X_0 = 0.65 \text{ kg kg}^{-1}$ ), gas flow rate ( $125 \text{ kg h}^{-1}$ ) and gas inlet temperature ( $80^\circ\text{C}$ ). The latter corresponds to an adiabatic saturation moisture content of  $Y_{as} = 22.3 \text{ g kg}^{-1}$ . Additional process parameters are summarized in Tab. 1.8. In the model equations, the particle flow rate  $\dot{N}_0$  and mean residence time  $\bar{\tau}$  are affected. Furthermore, an increase in particle flow rate increases the moisture load of the dryer, resulting in an increase in moisture content in the gas phase. Both effects cause a change in particle moisture content distribution and need to be considered.

The presented analytical model contains the model parameter  $p$  to adjust the shape of the normalized drying curve to the respective material. As discussed in the previous sections, the drying curve needs to be derived from experimental data. In this study, such measurements were carried out in the magnetic suspension balance. Single particle drying was performed at a gas inlet temperature of  $40^\circ\text{C}$ , a gas inlet moisture content of  $0.633 \text{ g kg}^{-1}$  and a pressure of 1022 mbar. For these conditions, the adiabatic saturation moisture content is  $10.62 \text{ g kg}^{-1}$ . The gas flow rate was set to  $100 \text{ ml min}^{-1}$ , corresponding to a gas velocity of  $3.6 \text{ mm s}^{-1}$ . The drying curves for two different runs under the same process conditions are presented in Fig. 1.36.

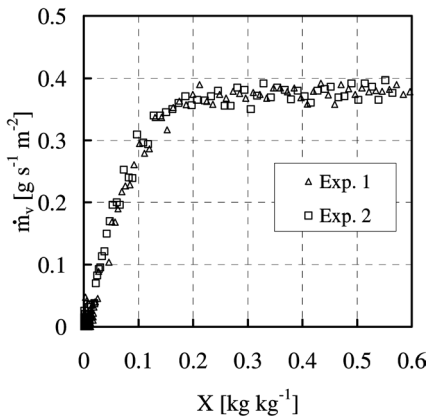


Fig. 1.36 Drying curves of  $\gamma\text{-Al}_2\text{O}_3$  particles ( $d_p = 1.8 \text{ mm}$ ) measured in MSB at  $T_{in} = 40^\circ\text{C}$ ,  $Y_{in} = 0.633 \text{ g kg}^{-1}$ ,  $Re = 0.38$ .

One can see that the drying rate is approximately constant at  $0.379 \text{ g s}^{-1} \text{ kg}^{-1}$  till a moisture content of about  $X=0.3$ . Assuming that this is the first period drying rate, we can also calculate it from Eq. 1.15. The mass transfer coefficient  $\beta$  can be determined from the Sherwood correlation of Eq. 1.59. For the given conditions the values,  $Sh=2.33$  and  $\beta=0.038 \text{ m s}^{-1}$  are obtained with a Reynolds number of  $Re=0.38$ . In turn, a drying rate of  $\dot{m}_{v,I} = 0.433 \text{ g s}^{-1} \text{ m}^{-2}$  is estimated from Eq. 1.15, which is somewhat higher than the measured value.

This slight difference can have several reasons. First, the Sherwood number can be smaller than calculated due to non-ideal flow conditions. Figure 1.37 shows that – instead of using the previously discussed basket or needle – the single particle was placed in a wire hoop. This may inhibit gas flow and diffusion around the particle. For a Sherwood number of  $Sh=2$  one would obtain an evaporation rate of  $\dot{m}_{v,I} = 0.372 \text{ g s}^{-1} \text{ m}^{-2}$ , which matches perfectly the experimental data. Another explanation is the reduction of vapor pressure due to hygroscopicity of the material. This effect can be accounted for by modifying the normalization method and defining the (then not constant) first period drying rate as

$$\dot{m}_{v,I} = \rho_g \cdot \beta \cdot (Y_{\text{eq}}(X, T_p) - Y_{\text{in}}) \quad (1.22)$$

Here,  $Y_{\text{eq}}$  denotes the equilibrium moisture content resulting from the sorption isotherm  $X(\varphi)$ .

The modified normalization concept has been extensively discussed by Burgschweiger *et al.* (1999) and applied successfully by subsequent authors (e.g. Burgschweiger and Tsotsas, 2002), but it is too complex for use with the present analytical model. Therefore, conventional normalization after van Meel (1958) is used here. In



Fig. 1.37 Suspended  $\gamma\text{-Al}_2\text{O}_3$  particle ( $d_p = 1.8 \text{ mm}$ ) for determination of single particle drying curve in the MSB.

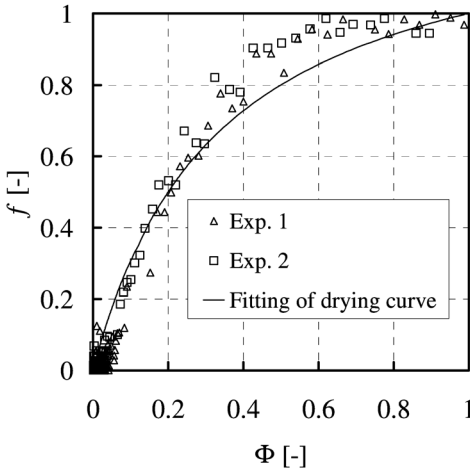


**Fig. 1.38** Normalized drying curve for  $\gamma\text{-Al}_2\text{O}_3$  particles ( $d_p = 1.8 \text{ mm}$ ,  $X_{cr} = 0.3$ ) and fitting by means of Eq. 1.14 with  $p = 4$ .

this frame, a critical moisture content of  $X_{cr} = 0.3$  is read from the single particle data of Figure 1.36 and the evaporation rate of the first drying period is determined from Eq. 1.15 with  $Sh = 2$ . The equilibrium moisture content  $X_{eq}$  is derived from the sorption isotherm provided by Groenewold *et al.* (2000). In this way, the normalized data of Fig. 1.38 are obtained for the test material.

To calculate moisture distributions for the dried solids from Eq. 1.16, one needs to fit the drying curve according to Eq. 1.14 by adjusting the parameter  $p$ . The result of this fitting is also depicted in Fig. 1.38. For dimensionless moisture contents  $\Phi > 0.5$  the fitting does not represent the experimental data very well, due to the symmetric shape of the curve according to Eq. 1.14. This drawback is a natural price to be paid for applying an analytical solution that does not allow for an arbitrary functional approximation of the normalized drying curve. Anyway, it is sufficient to justify the method, including its experimental background, as the final results will show.

Another crucial model parameter is  $K$ . According to Eq. 1.18,  $K$  depends on the diameter and density of the particle, the gas density and the adiabatic saturation moisture, which can all be either measured or calculated. Furthermore, it depends on the gas-side mass transfer coefficient in the fluidized bed. For this coefficient several models have been suggested in the literature. In the present study we applied a Sherwood correlation recommended by Burgschweiger and Tsotsas (2002), where axial dispersion in the gas is considered in the kinetic coefficient. Finally,  $K$  depends on the moisture content in the gas bulk,  $Y$ . To predict this moisture content, a model for the gas phase is required (ideal back-mixing, simple plug flow or some more complicated model). However, and in order to keep the present approach analytical, the parameter  $K$  was determined simply by fitting to the experimental results. In Tab. 1.8 the obtained values for  $Y$  and  $K$  are provided.

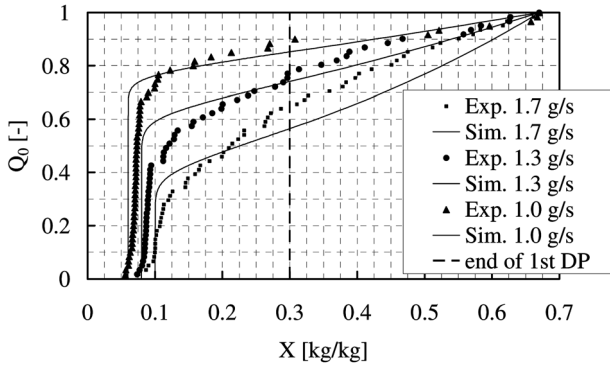


**Fig. 1.39** Comparison of the experimental and calculated distributions of solids moisture at the outlet of a continuous fluidized bed dryer for different particle flow rates (parameters according to Tab. 1.8).

Distributions measured at different particle flow rates and distributions calculated by Eq. 1.16 are plotted in Fig. 1.39. An increase in particle flow rate leads to a decrease in residence time and, consequently, to higher solids moisture contents. For higher particle flow rates (higher moisture loads) the gas moisture content  $Y$  increases (see also Tab. 1.8). Thus the relative humidity will increase, and the equilibrium state of the solids moves towards higher moisture contents. With the given set of parameters the experimental moisture distributions can be reproduced in a qualitatively satisfactory manner by the model. Deviations can be attributed to imperfect fitting of the normalized drying curve by Eq. 1.14. An extended model, incorporating the mass and energy balances for the solid and gas phase, would provide better agreement between experiments and simulation. However, the respective solutions are more complicated and, thus, less instructive than the here presented simplifications.

## 1.5 Acoustic Levitation

### 1.5.1 Introductory Remarks

The free suspension of a small droplet or particle near a pressure node of a standing acoustic wave is called *acoustic* or *ultrasonic levitation*. The gravitational force acting on the sample is compensated by the sound pressure of the ultrasonic field acting in a net upwards direction. The first systematic description of acoustic levitation was published by King (1934). In the 1970s the American space agency became interested in this phenomenon as a tool for containerless processing under microgravity conditions. Currently acoustic levitation is applied to examine the

drying behavior of suspended droplets and particles in the fields of chemistry, engineering and pharmacy. One central question when considering acoustic levitation is whether the sound pressure *per se* influences the drying behavior of a droplet or particle suspended in a standing wave? Although some work indicated that this influence may be negligible (Seaver *et al.*, 1989; Tian and Apfel, 1996), more recent studies have demonstrated and provided a theoretical background for the perturbation of droplet drying rate by an acoustic field (Yarin *et al.*, 1999). The most recent advances in this technique include the application of IR-thermography to measure the droplet surface temperature profile during drying (Tuckermann, 2002) and moisture detection in the exhaust gas stream using a dew point hygrometer (Groenewold *et al.*, 2002), compare with Section 1.2.1. One new application is the determination of the drying kinetics of aqueous solutions of proteins and carbohydrates (Schiffter and Lee, 2007a, b).

### 1.5.2

#### Some Useful Definitions

An acoustic field is characterized by its gas particle velocity and sound pressure. The gas particle velocity,  $B$ , is the velocity of a particle on a longitudinal pressure wave, given as the product of gas particle displacement,  $\zeta$ , and angular frequency,  $\omega$ :

$$B = \zeta \cdot \omega = \zeta \cdot 2\pi f \quad (1.23)$$

The sound velocity level (SVL or  $L_v$ ) gives the ratio of a gas particle velocity,  $B$ , to a standardized reference particle velocity,  $B_{\text{ref}}$ :

$$L_v = 20 \cdot \log \frac{B}{B_{\text{ref}}} \quad (1.24)$$

$B_{\text{ref}}$  is taken to be the lowest SVL detectable to the human ear, that is  $5 \times 10^{-8} \text{ m s}^{-1}$ . The unit of SVL is the decibel (dB) which is therefore dimensionless.

The sound pressure,  $P_{\text{sound}}$ , is that of the root-mean-square pressure deviation caused by a sound wave passing through a fixed point. It is the product of the medium density,  $\rho_0$ , the speed of the sound wave,  $u_0$ , and the gas particle velocity:

$$P_{\text{sound}} = \rho_0 \cdot u_0 \cdot B \quad (1.25)$$

Figure 1.40 illustrates how the sound pressure wave is  $\pi/2$  out of phase to the gas particle displacement wave. The logarithmic ratio of  $P_{\text{sound}}$  to a standardized reference sound pressure ( $P_{\text{ref}} = 2 \times 10^{-5} \text{ N m}^{-2}$ ) is called the sound pressure level (SPL or  $L_p$ ):

$$L_p = 20 \cdot \log \frac{P_{\text{sound}}}{P_{\text{ref}}} \quad (1.26)$$

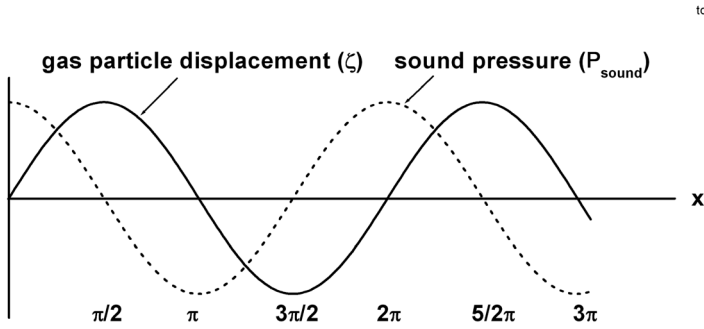


**Fig. 1.40** Shape of a horizontal sound pressure wave,  $P_{\text{sound}}$ , and its associated gas particle displacement wave,  $\zeta$ . Note that the  $P_{\text{sound}}$  is  $\pi/2$  out of phase with  $\zeta$ .

### 1.5.3

#### Forces in a Standing Acoustic Wave

A standing acoustic wave is formed within a closed tube whose length,  $L_r$ , is an integral multiple of the half-wavelength,  $\lambda/2$ , of the incident sound pressure wave:

$$L_r = n \cdot \frac{\lambda}{2}, \quad n = 1, 2, 3, \dots \quad (1.27)$$

The relation between the sound pressure wave's frequency,  $f$ , and the tube length is given by:

$$f = \frac{u_0}{\lambda} = n \frac{u_0}{2 \cdot L_r}, \quad n = 1, 2, 3, \dots \quad (1.28)$$

Interference of the incident and reflected sound pressure waves produces a series of nodes and anti-nodes in fixed positions. The gas particle displacement,  $\zeta$ , is zero at each node, and maximal at each anti-node, with the nodes and anti-nodes separated by a distance  $\pi/2$ . In an acoustic levitator (Fig. 1.41) a standing sound pressure wave is formed between an ultrasonic transducer at  $x=0$  (e.g. a piezo-crystal) which produces the incident wave, and a reflector placed at a distance  $L_r = n \lambda/2$  ( $n = 1, 2, 3, \dots$ ). A particle or droplet can be suspended or "levitated" in the vicinity of one of the sound pressure nodes, where the sound pressure acting upwards on the surface of the particle or droplet is positive and balances the gravitational force acting downwards.

King (1934) derived an expression for the sound pressure,  $P_a$ , exerted by a standing sound pressure wave in a gas of density  $\rho_0$ , at the surface of a rigid particle of radius  $a$ , and density  $\rho_1$ :

$$P_a = \pi \rho_1^C \sin(2\kappa h) f(\alpha) \quad (1.29)$$

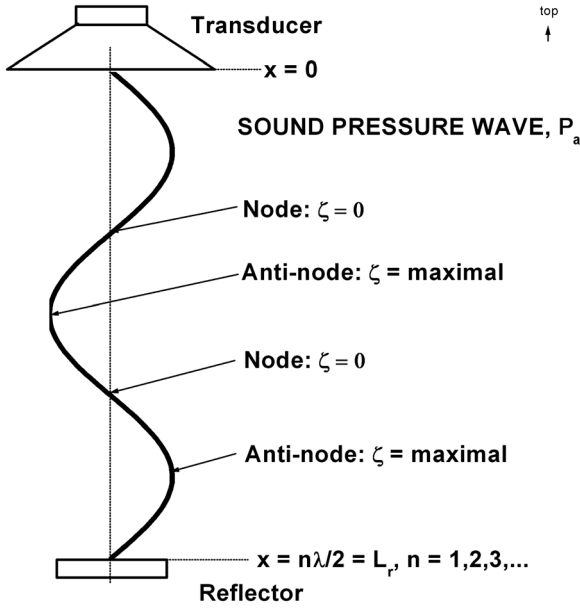


**Fig. 1.41** Representation of incident standing sound pressure wave formed between transducer and reflector in an acoustic levitator. At the pressure nodes the gas particle displacement is 0, whilst that at the empty nodes is a maximum.

where  $C_0$  (in  $\text{ms}^{-1}$ ) represents the constant of the solution applicable to the one-dimensional wave equation,  $\kappa$  is the wavenumber  $= \omega/u_0$ ,  $h$  is the displacement of the center of the spherical particle from a node at  $h = \pm n \times \pi/\kappa$ ,  $\alpha = \kappa a$ , and  $f(\alpha)$  is given by:

$$f(\alpha) = \frac{1}{\alpha^3} \frac{F_0 F_1 + G_0 G_1}{H_0^2 H_1^2} \alpha^2 - \frac{2}{\alpha^5} \frac{F_1 F_2 + G_1 G_2}{H_1^2 H_2^2} \{ \alpha^2 - 3(1 - \rho_0/\rho_1) \} + \sum_{n=2}^{\infty} (-1)^n \frac{n+1}{\alpha^{2n+3}} \frac{(F_{n+1} F_n + G_{n+1} G_n)}{H_n^2 H_{n+1}^2} \{ \alpha^2 - n(n+2) \} \quad (1.30)$$

The coefficients  $F_n$ ,  $G_n$ , and  $H_n$  are functions of  $\alpha$  and can be expressed as polynomials of  $1/\alpha^2$  (given by King, 1934) together with:

$$H_n^2(\alpha) = F_n^2(\alpha) + G_n^2(\alpha) \quad (1.31)$$

Equation 1.29 shows that the sound pressure acting on the particle in the standing wave is periodic and varies with the relative position of the center of the sphere to the nodes and anti-nodes. This behavior differs therefore from the sound pressure acting on a particle in a translating sound pressure wave, which is always positive.

Additionally, the sound pressure in the standing wave is much stronger than that in a translating wave. The standing sound pressure wave can therefore levitate a given droplet or particle, with its position relative to the nodes and anti-nodes depending on the wave's amplitude and also on the particle's radius and the relative density,  $\rho_0/\rho_1$ .

The acoustic levitation of a deformable droplet – relevant for droplet drying studies – was analyzed by Yarin *et al.* (1998). A one-dimensional sound pressure wave is approximated by assuming an infinite levitator with sound pressure:

$$P_{\text{sound}} = A_{0e} e^{-i\omega t} \cdot \cos\left(\frac{\omega}{u_0} x\right) \tag{1.32}$$

where  $A_{0e}$  is the effective amplitude. Figure 1.42a shows this standing sound pressure wave with its nodes and anti-nodes. In this representation it is  $x = z + L$  to take account of the vertical displacement,  $L$ , of the center of the spherical droplet at  $z = 0$  from the adjacent anti-node at  $x = 0$ . The positions of the nodes and anti-nodes are therefore:

$$\begin{aligned} \text{nodes}(\zeta = 0) : x = z + L &= \pm \frac{u_0}{\omega} \left( n\pi + \frac{\pi}{2} \right) \quad n = 0, 1, 2, \dots \\ \text{anti-nodes} : x = z + L &= \pm \frac{u_0}{\omega} n\pi \quad n = 0, 1, 2, \dots \end{aligned} \tag{1.33}$$

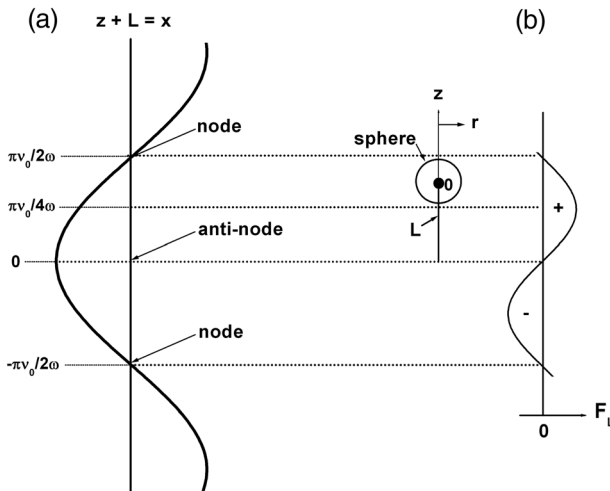


**Fig. 1.42** Representation of incident standing acoustic wave taken from Yarin *et al.* (1998). (a) The positions of the nodes and anti-nodes in the sound pressure wave calculated from the numerical solution of Yarin *et al.* (1998). (b) The acoustic levitation force,  $F_L$ , in dependence on both  $x$  and  $L$ , the distance between the center of the sphere and the adjacent anti-node. Note the region of positive acoustic levitation force.

The effective amplitude,  $A_{0e}$ , is selected to make Eq. 1.32 consistent with a levitator tube length of  $L_r$ , yielding:

$$A_{0e} = -\frac{A_0}{\cos(\omega L_r / u_0)} \quad (1.34)$$

$A_0$  is the amplitude at the transducer surface, that is  $x = 0$ . The approximated standing sound pressure wave described by Eqs. 1.32 and 1.34 gives node positions that are at most 5% removed from the exact solution for a levitator tube length of  $L_r$  (Yarin *et al.*, 1998).

This standing sound pressure wave is disturbed by the presence of a droplet levitated in the vicinity of one of the nodes, resulting in an additional scattered sound pressure wave:

$$P_{\text{sound}}^s = A_{0e} \cdot e^{-i\omega t} \cdot \bar{P}_s(r) \quad (1.35)$$

where the dimensionless function  $\bar{P}_s(r)$  of the radius vector  $r$  is found from the Helmholtz equation:

$$\nabla \bar{P}_s + \left(\frac{\omega}{u_0}\right)^2 \bar{P}_s = 0 \quad (1.36)$$

The total sound pressure existing at the sphere's surface is now the sum of the sound pressures of the incident wave,  $P_{\text{sound}}$ , plus the scattered wave,  $P_{\text{sound}}^s$ . Yarin *et al.* (1998) solved this problem by numerical evaluation of the associated boundary integral solutions to Eq. 1.36, and obtained the total sound pressure acting at the droplet surface,  $P_a$ . The resulting acoustic levitation force,  $F_L$ , was then obtained by integrating  $P_a$  over the droplet from top to bottom. Their numerical result for  $F_L$  in dependence on  $L$  could then be compared with the analytical result given for  $F_L$  from King's Eq. 1.29 in terms of  $L$ :

$$F_L = \pi \rho_0 \cdot \alpha^2 \cdot \left(\frac{A_{0e}}{\rho_0 \cdot u_0}\right)^2 \cdot \sin(2\alpha \cdot L) \cdot f(\alpha) \quad (1.37)$$

where  $f(\alpha)$  is as given in Eq. 1.30. The results in Tab. 1.9 illustrate the closeness of Yarin's approximation to King's analytical solution in Eq. 1.37. For a sound pressure wave of intermediate length ( $\alpha = 1$ ) the acoustic levitation force is positive in the

**Tab. 1.9** A comparison of the one-dimensional acoustic levitation force,  $F_L$ , existing along the standing sound pressure wave and acting on a sphere as calculated numerically by Yarin *et al.* (1998), and also from King (1934) analytical solution.  $F_L$  is rendered dimensionless by dividing with  $\rho_0 u_0^2 \alpha^2$ , and  $L$  by dividing with  $\alpha$ ;  $A_{0e}/\rho_0 u_0^2 = 1.0$ ,  $\alpha = 1.0$ , data taken from Yarin *et al.* (1998).

$L$	$F_L$ (Yarin <i>et al.</i> )	$F_L$ (King)
0	-0.0096	0
0.1	0.2737	0.2840
$\pi/4 = 0.785$	1.4148	1.4294
1.0	1.2849	1.2998
$\pi/2 = 1.55$	0.0466	0.0594

range of  $L$  between 0 and  $\pi/2$  (Fig. 1.42a), as predicted by Eq. 1.37. Furthermore, the maximum  $F_L$  exists at  $L = \pi/4$ . The numerical result differs from the analytical result by 1% (Yarin *et al.*, 1998).

For measurements with an acoustic levitator we must know at what sound pressure level acting at the sphere's surface,  $SPL_{\text{eff}}$ , the device is working.  $SPL_{\text{eff}}$  is directly related to the effective amplitude of the standing sound pressure wave,  $A_{0e}$  in  $\text{dyne cm}^{-2}$  (Yarin *et al.*, 1998):

$$SPL_{\text{eff}} = 20 \cdot \log(A_{0e}) + 74 \quad (1.38)$$

The sound pressure level at the sound source,  $SPL$ , is related to  $SPL_{\text{eff}}$  by using Eq. 1.34, to yield:

$$SPL = SPL_{\text{eff}} + 20 \cdot \log[-\cos(\omega \cdot L_r / u_0)] \quad (1.39)$$

Yarin *et al.* (1998) give two techniques for determining  $SPL_{\text{eff}}$  in a levitator. First, the “drop-out” method that determines  $A_{0e}$  by exploiting the balance of  $F_L$  from Eq. 1.37 and gravity acting on the sphere,  $F_G = 4/3 \pi a^3 \rho_1 g$ , that exists when the sphere is levitated stably at some point between  $L = 0$  and  $\pi/2$ . A sphere is levitated within the standing acoustic wave at known driving voltage,  $U_0$ , of the transducer.  $U_0$  is then reduced to the point  $U_{0m}$ , where the sphere drops out of the wave because  $F_L$  is now too small to compensate  $F_G$ . At this “drop-out point” the effective amplitude,  $A_{0em}$ , can be directly calculated from the properties of the levitated sphere:

$$A_{0em} = \left[ \frac{4}{3} \cdot \frac{a \cdot \rho_1 \cdot \rho_0 \cdot g \cdot u_0^2}{f(\alpha)} \right]^{1/2} \quad (1.40)$$

Providing the amplitude of the transducer varies linearly with  $U_0$ , then  $A_{0e}$  can now be determined from:

$$A_{0e} = A_{0em} \cdot \frac{U_0}{U_{0m}} \quad (1.41)$$

$SPL_{\text{eff}}$  is then directly available from Eq. 1.38 and is valid for the sphere size used in the experiment. The second technique calculates  $SPL_{\text{eff}}$  from the aspect ratio (= horizontal radius ( $r_h$ )/vertical radius ( $r_v$ )) of a levitated droplet. As we shall see in Section 1.5.4.1, a droplet suspended in an acoustic field will be deformed in shape by the asymmetric nature of the acoustic force acting on it. Yarin *et al.* (1998) used a numerical technique to solve the Bernoulli equation to give droplet shape as a function of  $P_a$ . By comparing measured aspect ratio with this solution the  $SPL_{\text{eff}}$  can be calculated at any time during droplet drying.

#### 1.5.4

##### Interactions of a Droplet with the Sound Pressure Field

A levitated droplet is influenced in its behavior by the standing sound pressure wave in four ways:

1. Deformation of the droplet, owing to anisotropic axial and radial levitation forces.

2. Acoustic streaming field near the surface of the levitated droplet which leads to acoustic convection and also solvent vapor accumulation, both of which phenomena greatly influence droplet drying rate.
3. Heating of the droplet, owing to oscillations of the ultrasonic transducer which change the temperature of the ambient drying air.
4. Increasing  $SPL_{\text{eff}}$  during evaporation as the droplet size decreases.

Any use of acoustic levitation to examine droplet or particle drying kinetics must recognize these effects.

#### 1.5.4.1 Deformation of Droplet Shape

A levitated droplet may deviate from a spherical shape because the sound pressure exerted by the standing wave is not uniform over the surface of the sphere. The extent of shape distortion depends on droplet size, the surface tension of the liquid, and the sound pressure (Trinh and Hsu, 1986; Marston *et al.*, 1981). For example, a higher sound pressure/SPL produces greater distortion and therefore a higher aspect ratio at fixed droplet size (Trinh and Hsu, 1986). The problem of predicting levitated droplet shape in dependence on sound pressure,  $P_a$ , was first analyzed by Marston *et al.* (1981) for small deformations (Trinh and Hsu, 1986). Tian *et al.* (1993) extended this by including adjustment between the drop and its surrounding field; the acoustic force that causes drop distortion is itself modified by the change in droplet shape. Yarin *et al.* (1998) adopted a numerical iteration technique to satisfy the equilibrium of  $F_L$  and  $F_G$ :

$$-2\pi \int_{\text{top}}^{\text{bottom}} P_a \frac{\partial r}{\partial s} r ds = \frac{4}{3} \pi a^3 \rho_1 g \quad (1.42)$$

where  $P_a$  is a function of droplet shape and  $L$ . Figure 1.43 reproduces a graphical comparison of experimental data of aspect ratio versus  $P_{\text{sound}}$  taken from Trinh and Hsu (1986) with the predictions of Marston *et al.* (1981); Tian *et al.* (1993); Yarin *et al.* (1998). The deviation observed with Marston's prediction illustrates the importance of recognizing the coupling of droplet shape distortion with  $F_L$ .

Of particular interest is the distribution of  $P_a$  across the  $z$ -axis of the droplet surface shown in Fig. 1.44. At the top ( $z \sim 0.5$ ) and bottom ( $z \sim -1.2$ ) of the droplet it is  $P_a > 0$  and the droplet surface is compressed. In the equatorial range ( $-0.7 \leq z \leq 0.3$ ) it is  $P_a < 0$  and the droplet surface is stressed (Yarin *et al.*, 1998). The result will be an oblate spheroid shape of the originally spherical droplet (Tian *et al.*, 1993).

#### 1.5.4.2 Primary and Secondary Acoustic Streaming

The sound pressure field around a droplet levitated in the standing wave results in streaming of the gas. The solution of the equations for an unsteady compressible boundary layer in the gas near the droplet surface gives the velocity of this acoustic streaming,  $\langle u_{\text{acoustic}} \rangle$ , as the time-average of multiple cycles of the standing acoustic

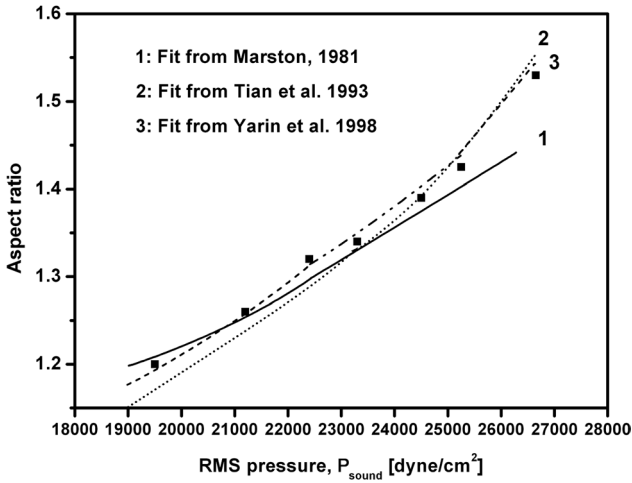


**Fig. 1.43** Influence of sound pressure on the aspect ratio of droplets of silicone oil levitated in an acoustic levitator ( $a_0 = 450 \mu\text{m}$ ,  $\alpha = 0.16$ ). The filled squares show the original experimental data taken from Trinh and Hsu (1986). The three curves represent the predictions given by Marston *et al.* (1981); Tian *et al.* (1993); Yarin, Paffenlehner and Tropea (1998). This figure has been redrawn from Yarin, Paffenlehner and Tropea (1998).

wave. The velocity field is illustrated in Fig. 1.45 (Yarin *et al.*, 1999) by the streamlines near the droplet surface. The distribution of  $\langle u_{\text{acoustic}} \rangle$  over the droplet surface is periodic, as seen in Fig. 1.46. In this representation  $x$  is the arc length of the droplet circumference measured from the bottom. The values of  $\langle u_{\text{acoustic}} \rangle$  given at  $x = 0$ ,  $x = x_2$  and  $x = x_3$  correspond to the points  $O_1$ ,  $O_2$  and  $O_3$  of the droplet surface shown

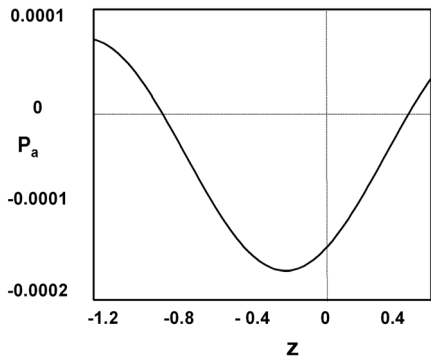


**Fig. 1.44** The distribution of sound pressure,  $P_a$ , acting on the droplet surface along the  $z$ -axis calculated for a n-hexane droplet of  $a_0 = 1061 \mu\text{m}$  at a transducer voltage of 156 V. Note the periodicity of  $P_a$  across the axis of the droplet surface, with  $P_a > 0$  at the top and bottom of the droplet. In the equatorial range  $P_a < 0$ . Figure reproduced from Yarin *et al.* (1998).

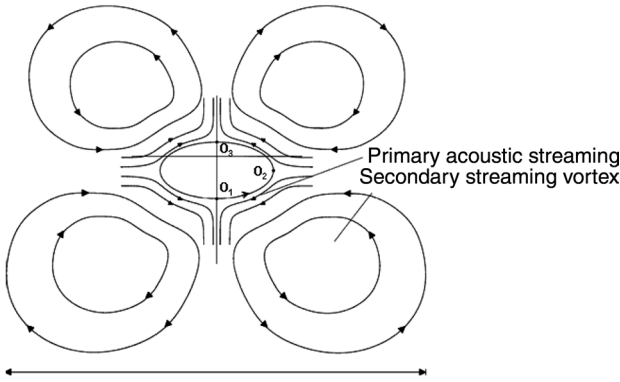


**Fig. 1.45** Sketch of the acoustic streaming field near a levitated droplet and the system of secondary toroidal vortices. The points O<sub>1</sub>, O<sub>2</sub> and O<sub>3</sub> refer to the calculated acoustic streaming velocities given in Fig. 1.46. This figure is taken from Yarin *et al.* (1999).

in Fig. 1.45. At the surface of the droplet a sound pressure boundary layer is thus formed by *primary acoustic streaming*. The radial thickness of this sound pressure boundary layer,  $\delta_{IAS}$ , is given by Yarin *et al.* (1999) and Lee and Wong (1990):

$$\delta_{IAS} = \left( \frac{2\nu_0}{\omega} \right)^{1/2} \quad (1.43)$$

where  $\nu_0$  is the kinematic viscosity of the gas. For the example of a water droplet of diameter  $d = 1.0$  mm levitated in air ( $\nu_0 = 1.5 \times 10^{-5} \text{ m}^2 \text{ s}^{-1}$ ) using a 56 kHz frequency transducer,  $\delta_{IAS} = 9.23 \mu\text{m}$  is obtained (Yarin *et al.*, 1999). This is much smaller than the diffusional boundary layer around the levitated droplet calculated to be  $92 \mu\text{m}$ ; but as we shall see later, its influence on droplet evaporation rate can be substantial.

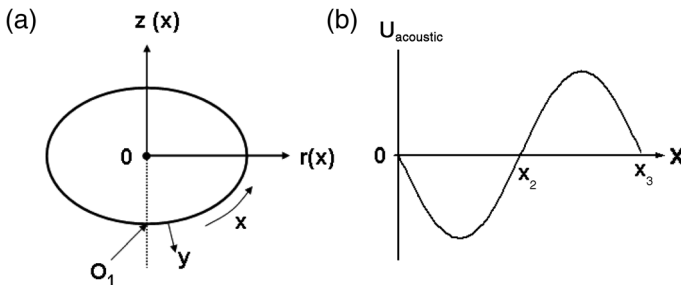


**Fig. 1.46** (a) Sketches of a levitated droplet showing its coordinates,  $x$ : the arc length of the droplets circumference from the bottom point O<sub>1</sub>,  $y$ : the normal to  $x$ . (b) The distribution of  $u_{acoustic}$  along the arc length,  $x$ , of the levitated droplet. The positions  $x = 0$ ,  $x = x_2$  and  $x = x_3$  represent the points O<sub>1</sub>, O<sub>2</sub> and O<sub>3</sub> in Fig. 1.45. Both graphs taken from Yarin *et al.* (1999).

Primary acoustic streaming results in an enhanced convection of solvent vapor away from the droplet surface. For a small spherical droplet where  $\kappa \gg 1$ , the solution for  $\langle u_{\text{acoustic}} \rangle$  reduces to (Yarin *et al.*, 1999; Burdukov and Nakoryakov, 1965):

$$\langle u_{\text{acoustic}} \rangle = -\frac{45}{32} \frac{B^2}{\omega \cdot a} \cdot \sin \frac{2x}{a} \quad (1.44)$$

For a water droplet levitated at an  $\text{SPL}_{\text{eff}}$  of 165.7 dB, Eq. 1.44 predicts a velocity of primary acoustic streaming of up to  $0.93 \text{ m s}^{-1}$  along the arc length of the droplet circumference (cf. Fig. 1.46) (Yarin *et al.*, 1999). This convective movement of the gas around the droplet must result in a Sherwood number,  $Sh > 2.0$ . Yarin *et al.* (1999) give the resulting distribution of the time-averaged  $Sh$  across the arc length  $x_1$  of the circumference of a small levitated droplet as:

$$\langle Sh \rangle = 2 \left( \frac{45}{4\pi} \right)^{1/2} \frac{B}{(\omega D_{10})^{1/2}} \cdot \frac{\cos^2(x_1/a)}{[1 + \cos^2(x_1/a)]^{1/2}} \quad (1.45)$$

The distribution of  $Sh$  is symmetrical about the vertical axis through point  $O_3$  in Fig. 1.45. The average  $Sh$  over the surface of the sphere is:

$$\langle \overline{Sh} \rangle = K_{\text{acoustic}} \cdot \frac{B}{(\omega \cdot D_{10})^{1/2}} \quad (1.46)$$

where  $D_{10}$  is the binary diffusivity of the solvent vapor in the gas, and  $K_{\text{acoustic}}$  is approximated by:

$$K_{\text{acoustic}} = \frac{2}{\sqrt{\pi}} \frac{|\langle \overline{u_{\text{acoustic}}} \rangle| \bar{r}}{\left( \int_{\bar{x}_2}^{\bar{x}} \langle \overline{u_{\text{acoustic}}} \rangle \bar{r}^2 d\bar{x} \right)^{1/2}} \cdot \left( \frac{\omega \cdot a / u_0}{A_{0e} / (\rho_0 \cdot u_0^2)} \right)^{1/2} \quad (1.47)$$

The quantity  $r = a \sin(x/a)$  is the  $r$ -coordinate of the droplet (cf. Fig. 1.46) that is set dimensionless with the initial droplet radius  $a_0$ . The term  $u_{\text{acoustic}}$  is set dimensionless with the gas particle velocity,  $B$ , and  $|\langle \overline{u_{\text{acoustic}}} \rangle| \bar{r}$  is averaged over the droplet surface. As droplet shape and hence  $r$  will change continuously during evaporation,  $K_{\text{acoustic}}$  has to be re-calculated continuously during the drying process. The  $Sh$  deduced from Eq. 1.46 will therefore be a time-function during droplet evaporation. For a small spherical droplet a good approximation of  $Sh$  is, however, given by:

$$\langle \overline{Sh} \rangle = \left( \frac{45}{4\pi} \right)^{1/2} \cdot \frac{B}{(\omega \cdot D_{10})^{1/2}} \quad (1.48)$$

This illustrates how, because of primary acoustic streaming,  $Sh$  depends directly on gas particle velocity,  $B$ , and hence on SPL via Eq. 1.25. These equations do not consider liquid flow with the levitated droplet, which increases  $u_{\text{acoustic}}$  by up to 10%. The corresponding increase in  $Sh$  is, however, negligible for mass transfer considerations (Rensink, 2004).

The effects of *secondary acoustic streaming* on droplet evaporation rate are the opposite of that of primary acoustic streaming. Figure 1.45 illustrates that secondary

acoustic streaming consists of a system of toroidal vortices around the levitated sphere. This system is caused by interaction of the primary acoustic streaming pattern with the walls of the levitator tube, or by droplet displacement from the pressure node. Secondary acoustic streaming has been verified experimentally (Trinh and Robey, 1994) and the mathematical problem solved (Lee and Wong, 1990; Yarin *et al.*, 1999). In the vortices the solvent vapor from the evaporating droplet can accumulate. Kastner determined experimentally the large scale of the vortices (Kastner, 2001). For the example of ethanol the accumulation of solvent vapor in the vortices proceeded to saturation within 0.6 s for a 2  $\mu\text{l}$  droplet evaporating at 25  $^{\circ}\text{C}$ . This accumulation of solvent vapor in the vortices is predicted to decrease diffusional mass transfer from the droplet surface to the surrounding gas phase.

To overcome the hindering effect of secondary acoustic streaming on droplet evaporation rate a forced ventilation gas stream needs to be introduced along the levitator axis. The accumulated solvent vapor is now removed from the vortices by forced convection (Seaver *et al.*, 1989; Trinh and Robey, 1994). Yarin *et al.*, (1997) visualized a ventilation gas stream passing around a levitated 5  $\mu\text{l}$  n-hexadecane droplet inside an acoustic levitator at a  $\text{SPL}_{\text{eff}}$  of approximately 156 dB. The images reproduced in Fig. 1.47 show how a ventilation gas stream of orifice Reynolds number  $Re_0 = 70$  moving up the levitator axis is trapped by the vortices of secondary streaming. Increase in  $Re_0$  up to  $\geq 190$  is sufficient to prevent formation of the vortices, and the ventilation gas stream passes around the levitated droplet.

According to Rensink (2004), the minimal flow velocity of a ventilation gas stream necessary to neutralize the secondary acoustic streaming pattern by “blow-out” ( $u_{\text{vent}}$ ) is given by:

$$u_{\text{vent}} \geq \frac{A_0}{\rho_0 \cdot u_0} \quad (1.49)$$

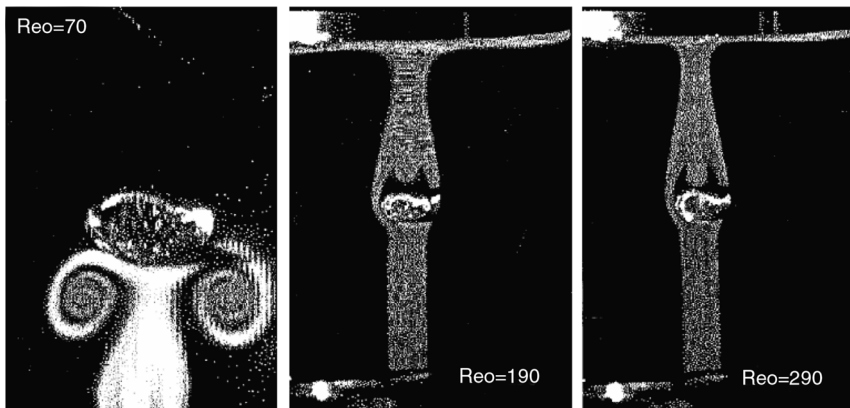


**Fig. 1.47** Utilization of ventilation gas stream passing through an ultrasonic levitator operating at  $\text{SPL}_{\text{eff}}$  of 156 dB. A 5  $\mu\text{l}$  n-hexadecane droplet is levitated and subjected to increasing ventilation gas velocity equivalent to orifice Reynolds numbers of  $Re_0 = 70, 190$  and  $290$ . Pictures taken from Yarin *et al.* (1997).

Recall that  $A_0$  is the amplitude of the sound pressure wave at the transducer source surface (Eq. 1.34). For a water droplet levitated at a SPL of 165.7 dB the predicted  $u_{\text{vent}}$  is  $4.3 \text{ m s}^{-1}$ . A ventilation gas velocity lower than  $u_{\text{vent}}$  can, however, be sufficient to prevent accumulation of solvent vapor in the toroidal vortices. This was shown to be true experimentally by Rensink (2004) for different solvent droplets.

#### 1.5.4.3 Effects of Changing Droplet Size

As elucidated in Section 1.5.4.1, a droplet levitated in a standing sound pressure wave is deformed to an oblate spheroid because the sound pressure acting on the droplet is not uniform along the sphere surface. During evaporation both the shape and the position of the droplet will, however, change. The droplet shape converges to that of a sphere (Kastner, 2001). The total pressure difference across the droplet surface comprises three parts (Tian *et al.*, 1993):

$$P_1 - P_o = \Delta P_s + \Delta P_G + \Delta P_{\text{st}} \quad (1.50)$$

where  $P_1$  and  $P_o$  are the pressures at the surface approached from the inside or outside, respectively;  $\Delta P_s$  is the contribution from the sound pressure wave,  $\Delta P_G$  is induced by gravity, and  $\Delta P_{\text{st}}$  is the difference in uniform static pressure inside and outside the droplet. In the absence of a sound pressure wave

$$\Delta P_{\text{st}} = 2\sigma/a \quad (1.51)$$

where  $\sigma$  is the surface tension of the liquid. Now, as the droplet shrinks during evaporation the decreasing radius of curvature will make  $\Delta P_{\text{st}}$  dominant over  $\Delta P_{\text{rad}}$  (Trinh and Hsu, 1986). The aspect ratio will therefore approach unity as the contribution from  $\Delta P_{\text{rad}}$  in Eq. 1.50 becomes less. Figure 1.48 shows experimental

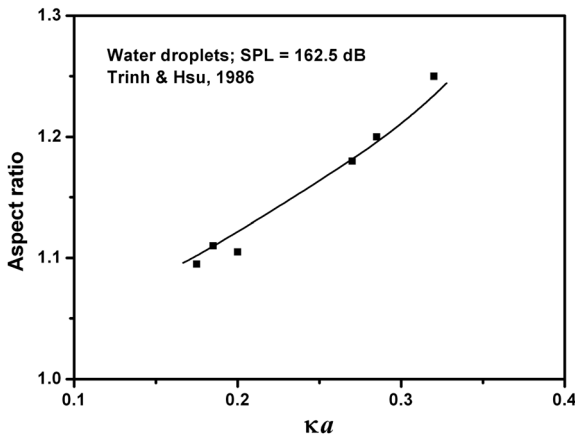


Fig. 1.48 Influence of shrinking droplet size on aspect ratio during evaporation;  $\kappa = \omega/u_0$ ,  $a$ : droplet radius). Data taken from Trinh and Hsu (1986).

data for evaporating water droplets. The decrease in  $\kappa a$  at fixed SPL causes the aspect ratio to decrease and approach unity.

Simultaneously the displacement of the droplet center from the nearest pressure node,  $\Delta z$ , decreases because the evaporating droplet rises in the standing sound pressure wave within the range  $0 < L < 2\pi$  (Yarin *et al.*, 1999). This is caused by a decreasing resonance shift of the levitator as droplet size decreases. When the droplet is introduced into the standing sound pressure wave it will immediately be deformed into an oblate spheroid (see Section 1.5.4.1). This change in droplet shape alters the scattered sound pressure wave, shifts hereby the resonance of the levitator, and decreases the sound pressure acting on the droplet surface,  $P_a$  (Trinh and Hsu, 1986). During evaporation the droplet size decreases and hence the resonance shift induced by the droplet will be progressively ameliorated. The result is a continual increase in  $SPL_{eff}$ , which returns to its unperturbed value when the droplet has disappeared. Figure 1.49 shows how the  $SPL_{eff}$  increases with decreasing droplet size during evaporation (Yarin *et al.*, 1998). The SPL needed to levitate the drop is directly proportional to the liquid's density,  $\rho_1$ . An increase in  $SPL_{eff}$  means, however, a higher gas particle velocity,  $B$ , and hence increased  $Sh$  in Eq. 1.46. This occurs during droplet evaporation in a sound pressure field and is expected to influence evaporation rate.

The decrease in droplet size during drying and the resulting increase in  $SPL_{eff}$  will raise  $F_L$  and cause a rise of the levitated droplet in the standing wave. Furthermore, as the mass of the levitated droplet decreases, the balance of gravitational and levitation forces,  $F_C$  and  $F_L$ , dictates that the droplet rises in the standing wave:

$$\frac{4}{3} \pi \cdot a^3 \cdot \rho_1 \cdot g = \pi \rho_0 \cdot a^2 \cdot \left( \frac{A_{0e}}{\rho_0 \cdot u_0} \right)^2 \cdot \sin(2\alpha \cdot L) \cdot f(\alpha) \tag{1.52}$$

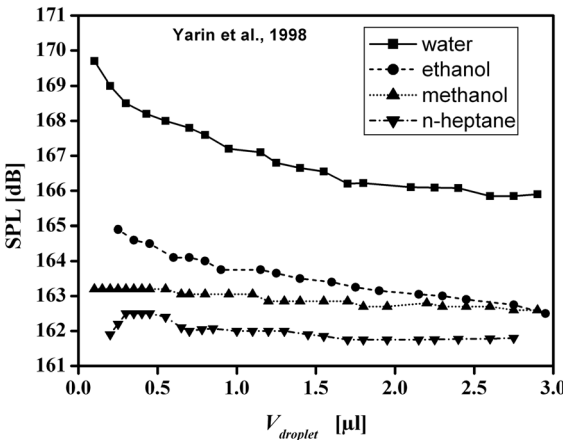


**Fig. 1.49** Increase in  $SPL_{eff}$  as droplet volume decreases during evaporation for four solvents. The  $SPL_{eff}$  was calculated from the change in the aspect ratio of the droplets during drying. Fig. taken from Yarin *et al.* (1998).

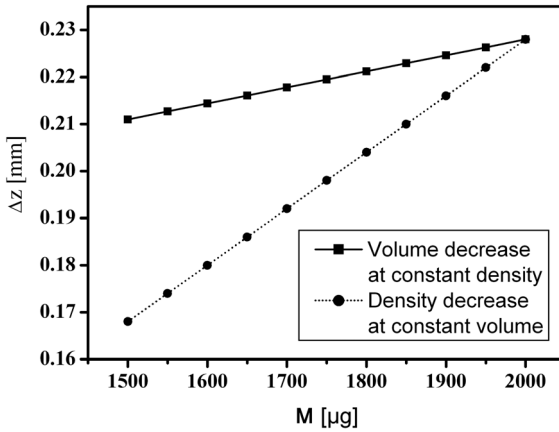


**Fig. 1.50** Position of droplet within sound pressure wave is dependence on its mass.  $\Delta z$  is the distance between the center of mass of the droplet and the adjacent pressure node. The upper line shows how  $\Delta z$  changes with decreasing volume at constant density. The lower line shows the behavior as density decreases at constant volume. These data were taken from Kastner (2001).

As droplet mass ( $4/3 \pi a^3 \rho_1$ ) decreases because of solvent evaporation, the sine function must decrease proportionately and the droplet rises within the sound pressure wave. Figure 1.50 taken from Kastner (2001) illustrates the influence of loss of mass on  $\Delta z$  of a droplet according to Eq. 1.52. A decrease in droplet volume at constant droplet density has a much weaker effect on  $\Delta z$  than does a decrease in density at constant volume.

In terms of drying of a solution droplet, the change in  $\Delta z$  is caused by progressive resonance amelioration and by decreasing droplet size till a solid porous particle has emerged (critical point). The subsequent change in  $\Delta z$  of the particle after the critical point is caused by change in density during solvent loss, since particle size now remains constant. This can be exploited to determine particle drying kinetics after the critical point (Yarin *et al.*, 1999; Kastner *et al.*, 2001).

## 1.5.5

### Single Droplet Drying in an Acoustic Levitator

#### 1.5.5.1 Drying Rate of a Spherical Solvent Droplet

Mass transfer from an evaporating droplet suspended in a gas phase was also discussed in Chapter 5, Vol. 1 of this series, in the context of spray dryer simulation. In general, two approaches can be applied. The first is to solve the conservation equations for a motionless sphere in an infinite stagnant medium, and to employ an empirical correction factor to account for forced convection around the droplet (Frohn and Roth, 2000). The second is to use film theory with analysis of the effects of forced convection on layer thicknesses for heat and mass transfer (Sirignano, 2000).

The first approach leads to the  $d^2$ -law and is a steady-state, gas phase model at constant temperature. A single, spherical droplet of initial radius  $a_0$  and fixed surface temperature,  $T_{ph}$ , is suspended in a still gas phase of fixed temperature  $T_\infty$ . At the droplet surface the saturation vapor pressure of the liquid,  $p^*$ , exists, whilst in the gas phase there is a lower vapor pressure,  $p_\infty$ . Solution of the one-dimensional diffusion equation for vapor flow rate at the droplet surface,  $\dot{M}_v$ , yields (Frohn and Roth, 2000):

$$\dot{M}_v = 4\pi \cdot D_{10} \cdot a(t) \{p^* - p_\infty\} \cdot \tilde{M} / (\tilde{R}T) \quad (1.53)$$

where  $D_{10}$  is the diffusivity of the vapor in the gas phase,  $\tilde{M}$  is liquid molecular mass, and  $\tilde{R}$  is the universal gas constant. The rate of shrinkage of the sphere,  $\dot{M}_{drop}$ , is given by:

$$\dot{M}_{drop} = 4\pi \cdot \rho_1 \cdot a^2(t) \cdot \frac{da}{dt} \quad (1.54)$$

Conservation of mass at the receding droplet surface specifies that:

$$\dot{M}_v = \dot{M}_{drop} \quad (1.55)$$

to yield for the time-profile of  $a(t)$ , otherwise known as the  $d^2$ -law:

$$a^2(t) = a_0^2 - \beta \cdot t \quad (1.56)$$

$$\beta = \frac{2D_{10}\tilde{M}}{\rho_1\tilde{R}} \left\{ \frac{p^*}{T_{ph}} - \frac{p_\infty}{T_\infty} \right\} \quad (1.57)$$

Droplet lifetime,  $t_1$ , is then given by:

$$t_1 = \frac{\rho_1 a_0 \tilde{R} (T_{ph} - T_\infty)}{2D_{10}\tilde{M} (p_{ph} - p_\infty)} \quad (1.58)$$

The  $d^2$ -law is valid in still gas, but can be corrected in an empirical fashion to account for forced convection of the gas phase. A good approximation is that of Ranz and Marshall (1952) determined for a suspended solvent drop:

$$\begin{aligned} Nu &= 2 + 0.6 \cdot Re^{1/2} \cdot Pr^{1/3} \\ Sh &= 2 + 0.6 \cdot Re^{1/2} \cdot Pr^{1/3} \end{aligned} \quad (1.59)$$

To describe the evaporation rate under forced convection conditions around a pure solvent droplet Eq. 1.57 is therefore changed to (Tuckermann *et al.*, 2002):

$$\beta = \frac{2D_{10}\tilde{M}}{\rho_1\tilde{R}} \left\{ \frac{p^*}{T_{ph}} - \frac{p_\infty}{T_\infty} \right\} \cdot \frac{Sh}{2} \quad (1.60)$$

The above equations do not account for any influences of the sound pressure field on gas movement around a levitated droplet, that is, acoustic streaming.

The alternative approach to droplet drying kinetics according to Sirignano (2000) is based on film theory to determine the radii,  $r$ , of the heat (index: t) and mass transfer (index: m) films around an evaporating sphere in a moving gas phase (forced convection):

$$\begin{aligned} r_{\text{film,t}} &= a \cdot \frac{Nu^*}{Nu^* - 2} \\ r_{\text{film,m}} &= a \cdot \frac{Sh^*}{Sh^* - 2} \end{aligned} \quad (1.61)$$

$Nu^*$  and  $Sh^*$  are the modified Nusselt and Sherwood numbers that account for the film thinning effects of Stefan flow:

$$\begin{aligned} Nu^* &= 2 + \frac{Nu - 2}{F_t} \\ Sh^* &= 2 + \frac{Sh - 2}{F_m} \end{aligned} \quad (1.62)$$

The correction factors  $F_t$  and  $F_m$  are functions of the film thicknesses for heat and mass transfer,  $\delta_t$  and  $\delta_m$ :

$$\begin{aligned} F_t &= \frac{\delta_t}{\delta_{t,0}} \\ F_m &= \frac{\delta_m}{\delta_{m,0}} \end{aligned} \quad (1.63)$$

$\delta_{t,0}$  and  $\delta_{m,0}$  are the initial film thicknesses at  $t = 0$ . The result of Abramzon and Sirignano (1989) for the time-profile of  $a(t)$  is analogous to Eq. 1.60:

$$a^2(t) = a_0^2(t) - \beta_{\text{film}} \cdot t \quad (1.64)$$

$$\beta_{\text{film}} = \frac{2 \cdot \rho_0 \cdot D_{10}}{\rho_1} \cdot \ln(1 - B_M) \cdot \frac{Sh^*}{2} \quad (1.65)$$

Here

$$B_M = \frac{\gamma_{\text{ph}} - \gamma_{\infty}}{1 - \gamma_{\text{ph}}} \quad (1.66)$$

is the Spalding transfer number that represents the driving force for vapor diffusion through a stagnant film (Frohn and Roth, 2000).  $\gamma$  is the mass fraction of solvent vapor in the gas. For a spherical droplet in an environment with no forced convection it is  $Sh = 2.0$ , and Eq. 1.66 simplifies to:

$$\beta_{\text{film}} = \frac{2 \cdot \rho_0 \cdot D_{10}}{\rho_1} \cdot \ln(1 - B_M) \quad (1.67)$$

which is directly analogous to the  $d^2$ -law. Again, these equations take no account of the influence of sound pressure field on evaporation rate.

### 1.5.5.2 Drying Rate of an Acoustically Levitated Solvent Droplet

The problem of determining the effect of a sound pressure wave on the evaporation rate of a levitated droplet was tackled by Yarin *et al.* (1999). For a small sphere the average  $Sh$  over the sphere surface is a function of gas particle velocity,  $B$ , as given by Eq. 1.48. Since  $Sh$  is defined as

$$\langle \overline{Sh} \rangle = \frac{k}{2a \cdot D_{10}} \quad (1.68)$$

where  $k$  is the time-averaged mass transfer coefficient at the droplet surface, it follows that

$$k = \frac{1}{2} \left( \frac{45}{4\pi} \right)^{1/2} \frac{B}{(\omega D_{10})^{1/2}} \cdot \frac{D_{10}}{a} \quad (1.69)$$

The vapor flow rate at the droplet surface,  $\dot{M}_v$ , is therefore:

$$\begin{aligned} \dot{M}_v &= 4\pi k a^2 (c_{ph} - c_\infty) \\ &= 2\pi a \left( \frac{45}{4\pi} \right)^{1/2} B \left( \frac{D_{10}}{\omega} \right)^{1/2} (c_{ph} - c_\infty) \end{aligned} \quad (1.70)$$

where  $c$  is the mass concentration of solvent vapor in the gas. Conservation of mass on equating Eq. 1.70 with the rate of shrinkage of the sphere,  $\dot{M}_{drop}$  in Eq. 1.54, gives:

$$a^2(t) = a_0^2 - \beta_{acoustic} \cdot t \quad (1.71)$$

$$\beta_{acoustic} = \left( \frac{45}{4\pi} \right)^{1/2} B \left( \frac{D_{10}}{\omega} \right)^{1/2} \frac{c_{ph} - c_\infty}{\rho_1} \quad (1.72)$$

Since  $(c_{ph} - c_\infty) = \tilde{M}(p^* - p_\infty) / (\tilde{R}T)$  for an ideal gas:

$$\beta_{acoustic} = \left( \frac{45}{4\pi} \right)^{1/2} \frac{B\tilde{M}}{\rho_1\tilde{R}} \left( \frac{D_{10}}{\omega} \right)^{1/2} \left\{ \frac{p^*}{T_{ph}} - \frac{p_\infty}{T_\infty} \right\} \quad (1.73)$$

Equations 1.71 and 1.73 are analogous to the  $d^2$ -law Eqs. 1.56 and 1.57 with the influence of primary acoustic streaming,  $u_{acoustic}$ , being accounted for. The droplet lifetime,  $t_1$ , is given in this case by:

$$t_1 = \frac{\rho_1 a_0^2 \tilde{R} (T_{ph} - T_\infty)}{\{45 D_{10} / (4\pi\omega)\}^{1/2} B \tilde{M} (p^* - p_\infty)} \quad (1.74)$$

which is shorter than that predicted by the  $d^2$ -law by the factor given by Eq. 1.48 for  $Sh$ .

### 1.5.5.3 Drying Rate of Droplets of Solutions or Suspensions

The first drying period of a droplet of a solution or suspension resembles that of a pure solvent droplet. It can therefore be described by the same equations, but taking into account the lowering of the vapor pressure by the dissolved substance. The

temporal decrease in droplet volume,  $\Delta V$ , gives directly the evaporation rate during this “constant-rate” drying period (Kastner, 2001):

$$\dot{M}_{cr} = -\rho_1 \cdot \frac{\Delta V}{\Delta t} \quad (1.75)$$

Ignoring the effect of the dissolved substance,  $a^2(t)/a_0^2$  decreases linearly with time according to either Eq. 1.56 ( $d^2$ -law), Eq. 1.64 by Abramzon and Sirignano or Eq. 1.71. After the critical point has been reached, the volume of the particle now existing should remain constant (Sherwood, 1929). Continued evaporation of solvent from the particle decreases both its mass and its density. As discussed in Section 1.5.4, this will cause the particle to rise ( $\Delta z$  decreases) within the ultrasonic field to maintain the balance between  $F_L$  and  $F_G$  given by Eq. 1.52 at constant  $SPL_{eff}$ . This particle movement can be used to determine the quantity of solvent evaporated in the second drying period, provided the  $SPL_{eff}$  and hence  $A_{0e}$  does not change after the critical point, and is known. The evaporation rate in this “falling-rate” drying period is then given directly from Eq. 1.37 (Yarin *et al.*, 1999; Kastner *et al.*, 2001):

$$\dot{M}_{fr} = \frac{\pi \rho_0 a^2}{\Delta t g} \left[ \frac{A_{0e}}{\rho_0 \cdot u_0} \right]^2 f(\alpha) \{ \sin(2\alpha L_1) - \sin(2\alpha L_2) \} \quad (1.76)$$

determined from the droplet position at two times,  $L_1$  and  $L_2$ , separated by  $\Delta t$ . Once  $\dot{M}_{fr}$  is known, the mean particle density,  $\rho_p$ , the mean moisture mass fraction of the droplet,  $x_1$ , and the mean particle porosity,  $\varepsilon$ , can be calculated as time-functions (Kastner *et al.*, 2001):

$$\begin{aligned} \rho_p(t) &= \frac{M_1(t) + M_s}{V_p} \\ x_1(t) &= \frac{M_1(t)}{M_1(t) + M_s} \\ \varepsilon(t) &= 1 - \frac{M_s}{\rho_s \cdot V_p} \end{aligned} \quad (1.77)$$

Ultrasonic levitation is therefore one of the few techniques suitable for examining the drying process of a solution droplet during both drying periods. The evaporation rate ( $\dot{M}_{cr}$  or  $\dot{M}_{fr}$ ) and residual solvent mass fraction ( $x_1$ ) of a droplet/particle can be determined at any desired point of time during evaporation. Furthermore, a droplet or particle can be removed from the levitation tube at any time for further analysis.

### 1.5.6

#### A Case Study: Single Droplet Drying of Water and an Aqueous Carbohydrate Solution

Recent studies of the drying behavior of levitated single droplets include pure solvents (Tuckermann *et al.*, 2002), inorganic colloidal solids (Kastner *et al.*, 2001), enzymes (Weis and Nardozi, 2005), and surfactants (Frost *et al.*, 1994). A study of

water and an aqueous solution of a carbohydrate useful in drug delivery (Schiffert and Lee, 2007a, b) illustrates the strengths and also the limitations of such experiments with an acoustic levitator. We present some selected results.

#### 1.5.6.1 A Typical Acoustic Levitator

A standard levitation system based on a published design (Yarin *et al.*, 1999) is shown in Fig. 1.51. A 58 kHz levitator is fixed within a plexiglas chamber, with the piezoelectric transducer in the roof and the reflector in its base. A drying gas is introduced into the levitator chamber through a hole in the center of the reflector, and is conditioned using a controlled evaporation mixer (CEM). A liquid flow controller type L1-FAC-33-0 humidifies the drying gas to  $0.2\text{--}10.0\text{ g}_{\text{water}}\text{ h}^{-1}$ . A gas flow controller type F-201C-FAC adjusts the drying gas flow rate to between 0 and  $2.01\text{ min}^{-1}$ . The drying gas temperature  $T_{\infty}$  is adjusted in the mixing unit W-202-330-T to produce the conditioned drying gas stream. The image of a levitated droplet is recorded continually using a JAI CF-M4 2/3 monochrome CCD camera with bellows and a Nikon 60 mm macrolens 0.8 diameter frame connected to a PC via a PcDIG LVDS frame grabber (32 bit). Images are recorded and analyzed using Image Pro Plus software version 4.51 (Media Cybernetics).

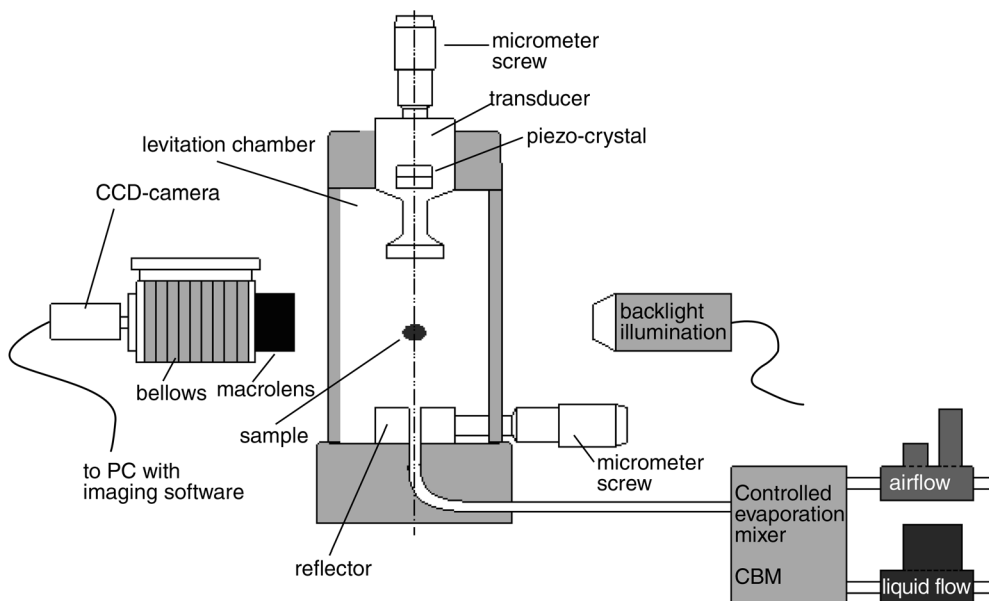


**Fig. 1.51** Design of an acoustic levitation system for measuring droplet drying kinetics and development of particle morphology. The plexiglas levitation chamber is covered by a plexiglas cover not shown in this illustration.

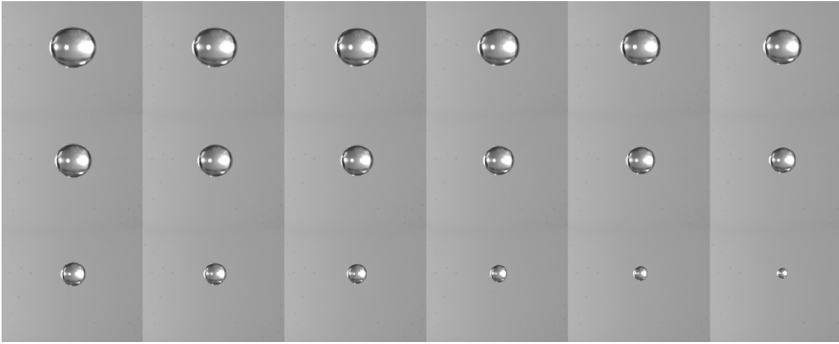


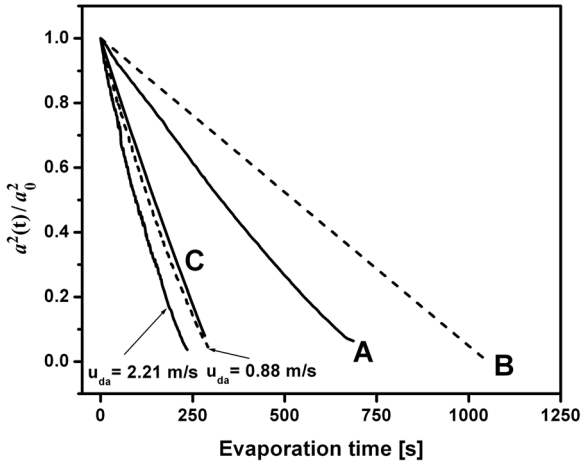
**Fig. 1.52** Photographic sequence of droplet appearance during drying in the acoustic levitator. This droplet is of pure water of initial diameter approximately  $500\ \mu\text{m}$  drying at  $T_\infty = 40^\circ\text{C}$  in still air at an  $\text{SPL}_{\text{eff}}$  of 162.47. The oblate spheroid shape of the droplet is evident from these photographs.

### 1.5.6.2 Evaporation Rates of Acoustically-Levitated Pure Water Droplets

Figure 1.52 shows a typical sequence of droplet profiles obtained for pure water of  $a_0 \cong 500\ \mu\text{m}$  drying at  $T_\infty = 40^\circ\text{C}$ , 0% RH and a drying air flow rate,  $u_{\text{da}}$ , of  $0\ \text{m s}^{-1}$ . The  $\text{SPL}_{\text{eff}}$  of 162.47 (at  $20^\circ\text{C}$ ) required to levitate this droplet size results in the oblate spheroid shape evident in these photographs. From measurements of the vertical and horizontal diameters,  $d_v$  and  $d_h$ , a surface-equivalent radius is calculated and plotted in Fig. 1.53 as  $a^2(t)/a_0^2$  versus evaporation time,  $t$  (labeled plot A).

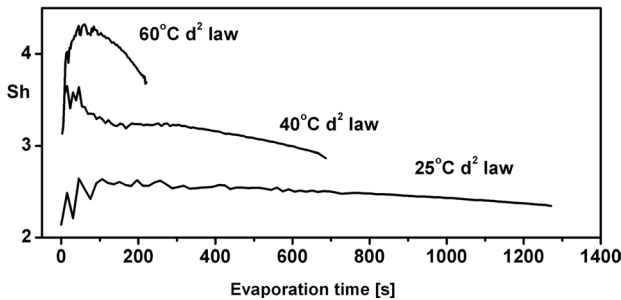
Figure 1.53 also contains the profile predicted for water under these conditions using Eqs. 1.56 and 1.57 according to the  $d^2$ -law (labeled plot B). For this calculation  $T_{\text{ph}}$  was taken to be the adiabatic saturation temperature,  $T_{\text{as}}$ ,  $p_\infty$  was taken to be zero (sink condition) and  $p^*$  was set to the value for the saturated water vapor pressure at  $T_{\text{as}}$ . The measured rate of evaporation (plot A) is clearly higher than that predicted by the  $d^2$ -law (plot B). The deviation from the  $d^2$ -law is quantified using Eq. 1.60 to calculate the Sherwood number at each time point of the experimental plots. The resulting temporal course of the fitted  $Sh(t)$  is shown in Fig. 1.54 for three different  $T_\infty$  in which the maximum  $Sh(t)$  observed at  $T_\infty = 40^\circ\text{C}$  is 3.6, substantially larger than that of 2.0 for pure diffusion-controlled evaporation through a stagnant boundary-layer. This result clearly demonstrates the substantial influence of the sound pressure on the evaporation rate of droplets of this size over a wide temperature range.

Figure 1.53 also contains the profile calculated using Eq. 1.46 to account for the effects of primary acoustic streaming on  $Sh(t)$  (labeled plot C). Equation 1.46 also does not accurately predict the experimental data, since the measured evaporation rate (plot A) is now lower than that predicted (plot C). The evaporation rate determined in the levitator is higher than that predicted by the  $d^2$ -law, but lower than that expected by considering the effects of  $\langle u_{\text{acoustic}} \rangle$  on mass transfer. This phenomenon can be attributed to the reduction in mass transfer caused by secondary



**Fig. 1.53** Evaporation of single droplets of pure water in an acoustic levitator. Plots of change in relative radius with evaporation time. A: Experimental result; B: prediction according to  $d^2$ -law (Eqs. 1.56 and 1.57); C: prediction according to effects of primary acoustic streaming on Sherwood number (Eq. 1.46). The remaining plots are experimental results obtained using drying air ventilation at the flow rates  $u_{da}$ .

acoustic streaming around the droplet. Rensink (2004) demonstrated how a forced-ventilation gas stream flowing axially through a levitator chamber can attenuate this phenomenon. Figure 1.53 contains the experimental plots of  $a^2(t)/a_0^2$  versus  $t$  determined at two drying air flow rates,  $u_{da}$ , axially through the levitator chamber. Increasing  $u_{da}$  causes a higher droplet evaporation rate than that measured in still air, that is  $u_{da} = 0$ . Clearly, the use of a forced-convection drying air stream will increase the evaporation rate under all conditions. In Fig. 1.53 it is, however, the attenuation of secondary acoustic streaming that causes the higher evaporation rate at  $u_{da} = 0.88 \text{ m s}^{-1}$ . At this value of drying air flow rate there is now good agreement



**Fig. 1.54** The temporal variation of Sherwood number during single droplet drying at three different drying air temperatures. The Sherwood number was calculated by fitting Eq. 1.60 to the experimental data. Results taken from Schiffter and Lee (2007a, b).

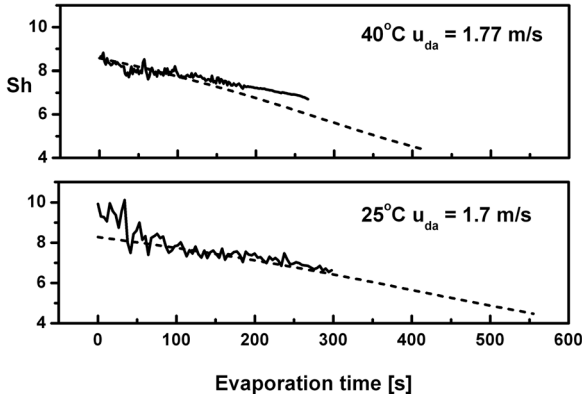


**Fig. 1.55** Measured and predicted values of Sherwood number for single droplet drying of pure water under conditions of drying air forced convection. The irregular plots are results obtained by fitting Eq. 1.60 to the experimentally determined values of droplet radius versus evaporation time. The straight lines are those predicted by Ranz and Marshall's correlation (Eq. 1.59). Data taken from Schiffter and Lee (2007a, b).

between the experimental plot and that predicted from Eq. 1.46 (plot C). According to Rensink (2004) this drying air flow rate prevents the accumulation of water vapor in the levitator tube by destroying the vortices and hence neutralizes the retarding effect of secondary acoustic streaming on the droplet evaporation rate.

If  $u_{da}$  is higher than that necessary to neutralize secondary acoustic streaming, then a further increase in evaporation rate is observed (Fig. 1.53 for the example  $u_{da} = 2.21 \text{ m s}^{-1}$ ). This additional, convection-driven evaporation can most conveniently be analyzed using Ranz and Marshall's correlation between  $Sh$  and  $u_{da}$  (Eq. 1.59). Figure 1.55 illustrates the example of  $u_{da} = 1.77 \text{ m s}^{-1}$  at  $T_{\infty} = 40^{\circ}\text{C}$  and  $u_{da} = 1.7 \text{ m s}^{-1}$  at  $25^{\circ}\text{C}$ . Reasonable agreement is obtained between the measured profiles of  $Sh(t)$  calculated by fitting Eq. 1.60 to the  $a(t)$ -profile and that predicted by Eq. 1.59. The experimental results are, however, only predicted accurately by Ranz-Marshall when  $u_{da}$  is higher than that value found necessary to neutralize secondary acoustic streaming. With lower values of  $u_{da}$  Eq. 1.59 is inaccurate, because the drying air stream in this flow range contributes to neutralizing an accumulation of solvent vapor within the vortices.

### 1.5.6.3 Evaporation Rates and Particle Formation with Aqueous Mannitol Solution Droplets

The sequence of photographs in Fig. 1.56 shows the drying of a single droplet of a 10 wt% aqueous solution of mannitol. The position of the critical point and subsequent particle formation can be seen. Figure 1.57 shows  $a^2(t)/a_0^2$  versus  $t$  for this system dried at  $T_{\infty} = 60^{\circ}\text{C}$  and 0% RH in still air. The plot is initially slightly concave to the  $x$ -axis up to a clear break at the critical point of drying  $t_{cp}$ . The droplet's aspect ratio decreases linearly up to the critical point, as  $\Delta P_{st}$  becomes more dominant in

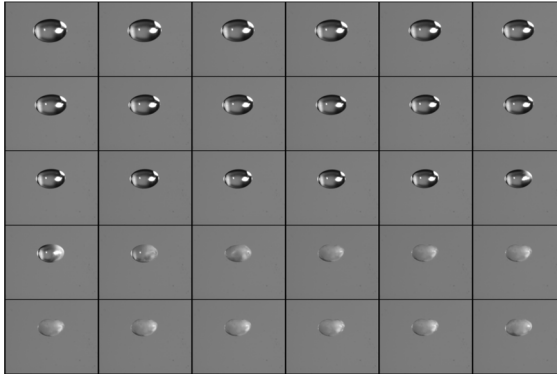


**Fig. 1.56** Sequence of photographs of drying of a single droplet of a 10wt% aqueous solution of mannitol at  $T_{\infty} = 60^{\circ}\text{C}$ . Note the oblate spheroid shape of the droplet and also the identifiable position of the critical point.

Eq. 1.50 with decreasing droplet size causing the droplet shape to converge to a sphere. At the critical point there is a sudden increase in aspect ratio which coincides with incipient formation of solid at the droplet surface. The critical point is thus clearly identifiable from the sharp changes occurring in both  $a^2(t)/a_0^2$  and the aspect ratio.

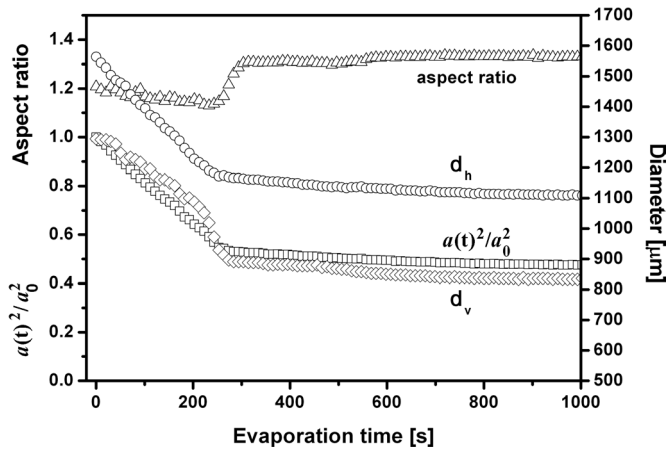


**Fig. 1.57** Results from single droplet drying of a 10wt% aqueous solution of mannitol at  $T_{\infty} = 60^{\circ}\text{C}$ . The plot of relative droplet/particle radius versus evaporation time shows a clear break point at the critical point. Also shown are the values for horizontal and vertical droplet/particle diameter,  $d_v$  and  $d_h$ . Data taken from Schiffter and Lee (2007b).

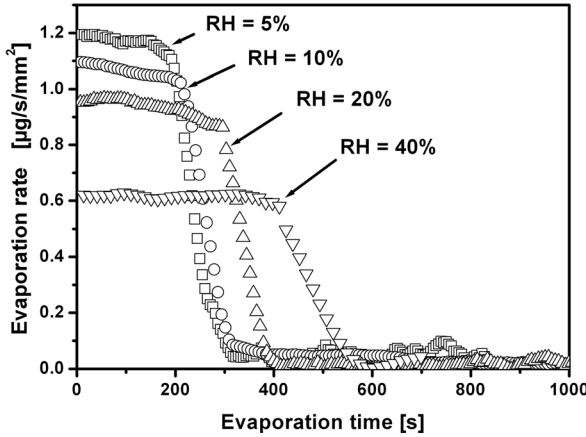


Fig. 1.58 Evaporation rate profiles for the single droplets of aqueous mannitol solution in dependence on the relative humidity of the drying air at  $T_{\infty} = 60^{\circ}\text{C}$ .

The droplet evaporation rate up to the critical point,  $\dot{M}_{\text{cr}}$ , is readily calculated from Eq. 1.75 and that after the critical point,  $\dot{M}_{\text{fr}}$ , from Eq. 1.76. In our experience  $\Delta z$  for use in Eq. 1.76 can be subject to substantial, erratic scatter. Indeed, Yarin *et al.* (1998) note that this parameter is highly sensitive, for example to horizontal displacements of the droplet in the standing sound pressure wave.

The evaporation rate profiles given in Fig. 1.58 show the influence of RH at  $T_{\infty} = 60^{\circ}\text{C}$  in still air. A clear distinction between the initial “constant-rate” and subsequent “falling-rate” periods is evident, with the position of the critical point being clearly identifiable. The value of  $\dot{M}_{\text{cr}}$  can be predicted from boundary-layer theory. For a spherical solution droplet evaporating in still drying air at constant temperature (Charlesworth and Marshall, 1960):

$$\dot{M}_{\text{cr}} = 2\pi\lambda_{\text{da}}d\Delta T/\Delta h_{\text{v}} \quad (1.78)$$

where  $\lambda_{\text{da}}$  is the thermal conductivity of the drying air at the droplet surface temperature,  $d$  is the mean average droplet diameter between  $t=0$  and  $t_{\text{cp}}$ ,  $\Delta T$  is the difference between the temperature of drying air,  $T_{\infty}$ , and the droplet surface temperature given by the adiabatic saturation temperature,  $T_{\text{as}}$ , and  $\Delta h_{\text{v}}$  is the enthalpy of evaporation of water. The evaporation time up to the critical point,  $t_{\text{cp}}$ , is then given by Schiffter and Lee (2007a, b):

$$t_{\text{cp}} = \Delta M_{\text{w,cr}}/\dot{M}_{\text{cr}} \quad (1.79)$$

where  $\Delta M_{\text{w,cr}}$  is the total mass of water lost between  $t=0$  and  $t_{\text{cp}}$ . This is given by  $4/3\pi(a_0^3 - a_{\text{cr}}^3)\rho_{\text{p}}x_{\text{w}}$ , with  $a_{\text{cr}}$  being the droplet/particle radius at the critical point and  $x_{\text{w}}$  the weight fraction of water in the solution.

The results in Tab. 1.10 show that the measured values for  $\dot{M}_{\text{cr}}$  are some three times larger than those predicted by Eq. 1.78. Consequently, the measured values for  $t_{\text{cp}}$  are much smaller than those predicted by Eq. 1.79. These discrepancies are a

**Tab. 1.10** Single droplet drying kinetics of aqueous mannitol 10 wt% ( $\rho_{m,0} = 100 \text{ kg m}^{-3}$ ) solution at drying air temperature  $T_\infty = 60^\circ \text{C}$  in still air ( $u_{da} = 0$ ). Symbols: RH = relative humidity of drying air;  $\dot{M}_{cr}$  = drying rate before critical point;  $t_{cp}$  = time to critical point;  $a_p$  = dry particle radius;  $a_0$  = initial droplet radius. Data taken from Schiffter and Lee (2007b).

RH [%]	Measured $\dot{M}_{cr}$ [ $\text{kg h}^{-1}$ ] $\times 10^{-6}$	Predicted $\dot{M}_{cr}$ [ $\text{kg h}^{-1}$ ] $\times 10^{-6}$	Measured $t_{cp}$ [s]	Predicted $t_{cp}$ [s]	$a_p/a_0$
5	29.3	8.95	202	503	0.59
10	26.5	8.33	234	554	0.57
20	23.5	7.22	332	669	0.53
40	15.2	5.27	453	950	0.49

consequence of the effect of  $\langle u_{acoustic} \rangle$  around the levitated droplet, as we have already seen in Section 1.5.6.2 with pure water. It is likely that these discrepancies between measured and predicted evaporation rates will depend on the initial  $\text{SPL}_{\text{eff}}$  required to levitate a particular droplet size. Tian and Apfel (1996) found, for example, no influence of a sound pressure field of low SPL of <150 dB on droplet evaporation rate and obtained a good agreement with Eqs. 1.56 and 1.57.

Lower  $\dot{M}_{cr}$  results in a decrease in the quotient of the dried particle to initial droplet radii,  $a_p/a_0$  (Tab. 1.10), at the same solids content. Since  $a(t)$  changes only marginally after the critical point, the value of  $a_p/a_0$  represents that size at which the precipitating mannitol forms a mechanically-stable crust at the droplet surface. The time to this point is shifted to longer values when  $\dot{M}_{cr}$  is reduced. If the droplet dries to a solid particle then  $a_p/a_0 = \sqrt[3]{\rho_{m,0}/\rho_s}$ , where  $\rho_s$  is the true density of the solid. A solid, fully-crystalline particle would fully dry to  $a_p/a_0 = 0.405$ . The measured values in Tab. 1.10 are all substantially higher than this theoretical result and give a quantitative measure of degree of particle porosity or hollowness. The drying behavior of the mannitol solution droplets is thus characterized by a sharp critical point caused by crystallization from a super-saturated surface solution, followed by a rapid decline in evaporation rate as moisture must now penetrate through the permeable crystalline crust.

## 1.6

### Concluding Remarks

The present chapter has presented experimental techniques such as:

- gravimetry by magnetic suspension balance
- dew point mirror hygrometry
- infrared spectroscopy
- nuclear magnetic resonance
- coulometry
- acoustic levitation.

With the help of examples, we have shown how these techniques can be used to:

- measure single particle drying kinetics
- determine kinetics of single drying droplets
- measure the distribution of moisture in a population of particles
- monitor the change of solids moisture content in convective dryers
- derive drying curves for the entire hold-up of dryers that can be scaled-down to single particle kinetics if an appropriate model is available.

What the discussed experimental techniques do not provide is resolution of the spatial distribution of moisture in drying solids. Methods capable of delivering this information are the subject of Chapters 2–4.

### Additional Notation Used in Chapter 1

$A$	amplitude of pressure standing wave	$\text{kg m}^{-1} \text{s}^{-2}$
$a$	droplet radius	m
$B$	gas particle velocity	$\text{m s}^{-1}$
$B$	magnetic field strength	T
$B_M$	Spalding transfer number	—
$c$	mass concentration of vapor	$\text{kg m}^{-3}$
$F$	force	$\text{kg m s}^{-2}$
$F$	correction factor, function	—
$f$	frequency	$\text{s}^{-1}$
$h$	displacement	m or dimensionless
$K$	drying rate constant	$\text{s}^{-1}$
$L$	vertical displacement	m
$L_p$	sound pressure level (SPL)	—
$L_r$	tube length	m
$L_v$	sound velocity level (SVL)	—
$M$	magnetization	T
$\dot{N}$	particle flow rate	$\text{s}^{-1}$
$p$	shape parameter of drying curve	—
$Q$	normalized cumulative number density	—
$Q$	electric charge	C
$T$	relaxation time	s
$U$	voltage	V

### Greek letters

$\alpha$	wavenumber times particle radius	—
$\beta$	droplet evaporation constant	$\text{s}^{-1}$
$\delta$	boundary layer thickness	m
$\zeta$	gas particle displacement	m
$\kappa$	wavenumber	$\text{m}^{-1}$

$\lambda$	wavelength	m
$\tau$	residence time	s
$\omega$	angular frequency	$s^{-1}$

### Subscripts and superscripts

a	acoustic
BL	balance display without sample
BLS	balance display with sample
cp (or: cr)	critical point
cr (or: I)	constant rate
da	drying air
e (or: eff)	effective
fr	falling rate
G	gravity
h	horizontal
IAS	acoustic boundary layer
L	load cage and basket
L	levitation
m	drop-out
m	mass transfer
S	sample
s	scattered
st	static
t	heat transfer
v	vertical
vent	ventilation
0	initial, inlet, driving
0 (or: g)	surrounding medium, gas
$\langle \rangle$	time-average over cycles
—	spatial average over droplet

### Abbreviations

FID	free induction decay
IR	infrared
LDE	light emitting diode
MSB	magnetic suspension balance
NMR	nuclear magnetic resonance
PRT	platinum resistance thermometer
RH	relative humidity
SPL	sound pressure level
SVL	sound velocity level
TLM	thin layer method

## References

- Abramzon, B., Sirignano, W. A., 1989. Droplet vaporization model for spray combustion calculations. *Int. J. Heat Mass Transfer* **32**: 1605–1618.
- Blumberg, W., 1995. *Selektive Konvektions- und Kontaktrocknung im Drehrohr*. Dissertation, Universität Karlsruhe, Germany.
- van Brakel, J., 1980. *Mass transfer in convective drying*. Mujumdar, A. S., Advances in drying, Hemisphere, New York, USA.
- Burdukov, A. P., Nakoryakov, V. E., 1965. On mass transfer in an acoustic field. *J. Appl. Mech. Tech. Phys.* **6**: 51–55.
- Burgschweiger, J., Tsotsas, E., 2002. Experimental investigation and modelling of continuous fluidized bed drying under steady-state and dynamic conditions. *Chem. Eng. Sci.* **57**: 5021–5038.
- Burgschweiger, J., Groenewold, H., Hirschmann, C., Tsotsas, E., 1999. From hygroscopic single particle to batch fluidized bed drying kinetics. *Can. J. Chem. Eng.* **77**: 333–341.
- Charlesworth, D., Marshall, W. 1960. Evaporation from drops containing dissolved solids. *AIChE J.* **6**: 9–23.
- DaSilva, F. A., Rodrigues, A. E., 1997. Equilibrium and kinetics of n-hexane sorption in pellets of 5A zeolites. *AIChE J.* **43**: 2524–2534.
- Frohn, A., Roth, N., 2000. *Dynamics of droplets*. Springer, Berlin, Germany.
- Frost, A. E., Seaver, M., Rubel, G. O., 1994. Delayed appearance of the liquid-condensed phase in 1-octadecanol films on levitated water drops. *J. Chem. Phys.* **100**: 3268–3275.
- Groenewold, C., Möser, C., Groenewold, H., Tsotsas, E., 2002. Determination of single-particle drying kinetics in an acoustic levitator. *Chem. Eng. J.* **86**: 217–222.
- Groenewold, H., 2004. *Wirbelschichtrocknung mit indirekter Beheizung*. Dissertation, Otto-von-Guericke-University Magdeburg, Germany.
- Groenewold, H., Tsotsas, E., 1997. A new model for fluidized bed drying. *Drying Technol.* **15**: 1687–1698.
- Groenewold, H., Tsotsas, E., 2007. Drying in fluidized beds with immersed heating elements. *Chem. Eng. Sci.* **62**: 481–502.
- Groenewold, H., Hirschmann, C., Burgschweiger, J., Tsotsas, E., 2000. Comparison of convective drying kinetics of active and inactivated  $\text{Al}_2\text{O}_3$ . *Bull. Pol. Acad. Sci.* **48**: 269–382.
- Hirschmann, C., Tsotsas, E., 1998. Impact of the pore structure on particle-side drying kinetics. *Proceedings of 11th International Drying Symposium*, Thessaloniki, 216–223.
- Hirschmann, C., Fyhr, C., Tsotsas, E., Kemp, I. C., 1998. Comparison of two basic methods for measuring drying curves: thin layer method and drying channel. *Proceedings of 11th International Drying Symposium*, Thessaloniki, 224–231.
- Kastner, O., 2001. *Theoretical and experimental studies of mass transfer from single droplets in an acoustic levitator*. Dissertation, Universität Erlangen, Germany.
- Kastner, O., Brenn, G., Rensink, D., Tropea, C., 2001. The acoustic tube levitator – a novel device for determining the drying kinetics of single droplets. *Chem. Eng. Technol.* **24**: 335–339.
- Keidel, F. A., 1959. Determination of water by direct amperometric measurement. *Anal. Chem.* **31**: 2043–2048.
- Kemp, I. C., Fyhr, B. C., Laurent, S., Roques, M. A., Groenewold, C., Tsotsas, E., Sereno, A. A., Bonazzi, C. B., Bimbenet, J. J., Kind, M., 2001. Methods for processing experimental drying kinetics data. *Drying Technol.* **19**: 15–34.
- Kettner, C., Peglow, M., Metzger, T., Tsotsas, E., 2006. Distributed product quality in fluidized bed drying. *Proceedings of 15th International Drying Symposium*, Budapest, Volume B, 745–750.
- King, L. V. 1934. On the acoustic radiation pressure on spheres. *Proc. R. Soc., London, Ser. A* **147**: 212–240.
- Kwapinski, W., Tsotsas, E., 2004a. Experimental determination of single-

- particle kinetics and equilibria for convective drying, desorption or adsorption by a magnetic suspension balance. *Proceedings of 14th International Drying Symposium*, Sao Paulo, Volume A, 1419–1426.
- Kwapinski, W., Tsotsas, E., 2004b. Determination of kinetics and equilibria for adsorption of water vapour on single particles by a magnetic suspension balance. *Chem. Eng. Technol.* **27**: 681–686.
- Kwapinski, W., Tsotsas, E., 2006. Characterization of particulate materials in respect to drying. *Drying Technol.* **24**: 1083–1092.
- Lee, C. P., Wong, T. G., 1990. Outer acoustic streaming. *J. Acoustic. Soc. Am.* **88**: 2367–2375.
- Looi, A. Y., Golonka, K., Rhodes, M., 2002. Drying kinetics of single porous particles in superheated steam under pressure. *Chem. Eng. J.* **87**: 329–338.
- Marston, P. L., Lo-Porto-Arione, S. E., Pullen, G. L., 1981. Quadrupole projection of the radiation pressure on a compressible sphere. *J. Acoustic. Soc. Am.* **69**: 1499–1501.
- van Meel, D., 1958. Adiabatic convection batch drying with recirculation of air. *Chem. Eng. Sci.* **9**: 36–44.
- Metzger, T., Klotchov, A., Vergeldt, F., van As, H., Tsotsas, E., 2005. Magnetic resonance imaging to monitor moisture profiles in a drying nano-porous sphere. *Proceedings of 7th World Congress of Chemical Engineering*, Glasgow, C14-004.
- Ranz, W., Marshall, W., 1952. Evaporation from drops. Parts I and II. *Chem. Eng. Prog.* **48**: 141–173.
- Rensink, D., 2004. *Evaporation of acoustically-levitated oscillating droplets of homogeneous and heterogeneous media*. Dissertation, Universität Erlangen, Germany.
- Rubotherm, 2004. *Magnetic Suspension Balance*. Bochum, Germany.
- Schiffert, H., Lee, G. W. J., 2007a. Single-droplet evaporation kinetics and particle formation in an acoustic levitator. Part 1: evaporation of water microdroplets assessed using boundary-layer and acoustic levitation theories. *J. Pharm. Sci.* **96**: 2284–2295.
- Schiffert, H., Lee, G. W. J., 2007b. Single-droplet evaporation kinetics and particle formation in an acoustic levitator. Part 2: drying kinetics and particle formation from microdroplets of aqueous mannitol, trehalose or catalase. *J. Pharm. Sci.* **96**: 2296–2309.
- Seaver, M., Galloway, A., Manuccia, T. J., 1989. Acoustic levitation in a free-jet wind tunnel. *Rev. Sci. Instrum.* **60**: 3452–3458.
- Sherwood, T. K., 1929. The drying of solids II. *Ind. Eng. Chem.* **21**: 976–980.
- Shibata, H., 2005. Comparison of drying rate curves of porous solids in superheated steam to those in air. *Drying Technol.* **23**: 1419–1434.
- Sirignano, W. A., 2000. *Fluid dynamics and transport of droplets and spray*. Cambridge University Press, Cambridge, UK.
- Suherman, 2007. *Drying kinetics of granular and powdery polymers*. Dissertation, Otto-von-Guericke-University Magdeburg, Germany.
- Suherman, Peglow, M., Tsotsas, E., 2008. On the applicability of normalization for drying kinetics. *Drying Technol.* **26**: 90–96.
- Tian, Y., Apfel, R. E., 1996. A novel multiple drop levitator for the study of drop arrays. *J. Aerosol Sci.* **27**: 721–737.
- Tian, Y., Holt, R. G., Apfel, R. E., 1993. Deformation and location of an acoustically levitated liquid drop. *J. Acoust. Soc. Am.* **93**: 3096–3104.
- Trinh, E. H., Hsu, C., 1986. Equilibrium shapes of acoustically levitated drops. *J. Acoust. Soc. Am.* **1335**–1338.
- Trinh, E. H., Robey, J. L., 1994. Experimental study of streaming flows associated with ultrasonic levitators. *Phys. Fluids* **6**: 3567–3579.
- Tsotsas, E., 1994. From single particle to fluid bed drying kinetics. *Drying Technol.* **12** (6): 1401–1426.
- Tuckermann, R., 2002. *Gase, Aerosole, Tropfen und Partikel in stehenden Ultraschallfeldern*. Dissertation, Universität Braunschweig, Germany.

- Tuckermann, R., Bauerecker, S., Neidhart, B., 2002. Evaporation rates of alkanes and alcohols from acoustically levitated drops. *Anal. Bioanal. Chem.* **372**: 122–127.
- Weis, D. D., Nardozi, J. D., 2005. Enzyme kinetics in acoustically levitated droplets of supercooled water: a novel approach to cryoenzymology. *Anal. Chem.* **77**: 2558–2563.
- Yarin, A. L., Brenn, G., Keller, J., Pfaffenlehner, M., Ryssel, E., Tropea, C., 1997. Flowfield characteristics of an aerodynamic acoustic levitator. *Phys. Fluids* **9**: 3300–3314.
- Yarin, A. L., Pfaffenlehner, M., Tropea, C., 1998. On the acoustic levitation of droplets. *J. Fluid Mech.* **356**: 65–91.
- Yarin, A. L., Brenn, G., Kastner, O., Rensink, D., Tropea, C., 1999. Evaporation of acoustically levitated droplets. *J. Fluid Mech.* **399**: 151–204.

